

Impact of Ethanol and Methanol on NO_x Emissions in Ammonia–Methane Combustion: ReaxFF Simulations and ML-Based Extrapolation

Amirali Shateri, Zhiyin Yang, Jianfei Xie *

School of Engineering, University of Derby, DE22 3AW, UK

Abstract

The development of ammonia–methane (NH₃–CH₄) combustion as a hydrogen-carrier energy source faces major challenges such as significant NO_x emissions, hindering its practical implementation. This paper examines how ethanol (C₂H₆O) and methanol (CH₄O) additives influence formation pathways of NO_x using ReaxFF molecular dynamics (MD) simulations at temperatures of 2,000 K and 3,000 K. Ten carefully designed fuel mixtures (C1–C10) were evaluated across 0%, 5%, and 10% alcohol concentrations. The findings show that adding alcohol can effectively suppress NO_x production, especially at elevated temperatures. At 3,000 K, 10% ethanol addition and 10% methanol addition reduced the production of NO_x by approximately 39.6% and 30.1%, respectively, compared with the base fuel. This suppression is attributed to the charge redistribution and the redirection of nitrogen intermediates through stabilising pathways such as HNO, HNO₂, and N₂O. Simulation-derived descriptors served as the training data for machine learning (ML) models, including Random Forest Regression (RFR), Support Vector Regression (SVR), Gradient Boosting Regression (GBR), and Fully Connected Neural Networks (FCNN). RFR achieved superior performance compared with other models with an R² of 0.993 and mean absolute error (MAE) of 0.661. The trained ML models successfully predicted NO_x emissions for both simulated alcohol ratios (0%, 5% and 12%), and non-simulated alcohol ratios (2%, 7%, and 12%) which demonstrating how hybrid physics-informed ML algorithms can extrapolate complex chemical behaviours, along with prediction errors under 5% for most extrapolated ethanol cases. The results showcase that the ReaxFF informed ML framework successfully serves as a basis for designing cleaner fuels and is capable of establishing a reliable structure for future predictive models in combustion chemistry.

Keywords: NO_x emission; Ammonia–methane combustion; Alcohol additives; Machine learning; Reactive force field; molecular dynamics.

1. Introduction

Growing worldwide demand for sustainable energy sources promotes the use of fuels with low carbon emissions and carbon-neutral options. Ammonia (NH₃) represents a feasible option for hydrogen transportation and fuel application since it burns carbon-neutrally and can integrate with existing infrastructure [1-2]. The slow reaction kinetics combined with low laminar burning velocity and high ignition temperature make NH₃ difficult to use as a standalone fuel. Blending ammonia with hydrocarbon fuels like methane (CH₄) has been recommended by researchers to overcome combustion challenges and improve burning process stability and efficiency [3]. Ammonia-methane fuel blends have emerged as promising candidates for low-emission energy systems, especially in high-temperature combustion applications [3]. These fuel blends are being explored for their potential to reduce the environmental impact of

*Corresponding author: j.xie@derby.ac.uk (J.X)

combustion processes by lowering harmful emissions, particularly nitrogen oxides (NO_x), which are a byproduct of fuel-bound nitrogen oxidation [4].

Recent research has revealed how NH₃ and CH₄ interact synergistically in mixed fuel systems and explored different NO_x reduction techniques. Liao et al. [5] demonstrated that CH₄ significantly shortens NH₃ ignition delay because it accelerates NH₃ oxidation through enhanced radical generation under different equivalence ratios and pressure conditions. Kohansal et al. [6] blended ammonia with methane to reduce the laminar burning velocity, but optimal conditions at high temperatures allowed these blends to achieve performance levels comparable to standard hydrocarbon flames with considerable effects on NO_x formation process. Studies on the combustion dynamics of NH₃/CH₄ mixes are conducted in conjunction with focuses on enhanced burner design. Singh et al. [7] used both computational models and experimental testing in a self-recuperative burner to show how different ammonia levels influence the behaviour of OH, HNO and HCO radicals, which in turn alters flame stability and emission levels of pollutants. Kim et al. [8] showed the use of non-thermal plasma to promote the streamer intensity and enhance the flame propagation in NH₃/CH₄-air mixtures, resulting in reduced emissions and better lean-burn performance. In addition, the autoignition characteristics have been investigated for high-temperature behaviour. Chu et al. [9] conducted a study on the ignition delay time of NH₃/CH₄ mixtures at temperatures ranging from 1,200 to 2,200 K, indicating consistent ignition performance at specific pressures with NH₃-dominant mixtures, thereby suggesting enhanced flame control capabilities for advanced combustion systems. Furthermore, Zhang et al. [10] revealed the unique chain-termination pathways of NH₃ in comparison to other fuels under various pressure conditions, contrasting with the high-pressure chemical behaviour of CH₄. Han et al. [11] developed empirical correlations between the diluent fraction and laminar burning velocity (SL) for NH₃-CH₄-N₂ mixtures based on the flame structure analysis.

Several studies have shown that incorporating alcohol-based additives into fuel mixtures effectively reduces pollutant emissions, including hydrocarbons (HC), carbon monoxide (CO), and nitrogen oxides (NO_x). Usman et al. [12] demonstrated that petrol blends containing ethanol and methanol achieved up to 13.2% reductions in HC emissions with E10 (10% ethanol in 90% of gasoline) blends. When traditional fuels are blended with alcohol fuels, it results in improved brake thermal efficiency (BTE). Pure petrol experienced a 2.35% BTE gain with E10 and a 1.53% with 5% ethanol and 5% methanol (E5M5) blends. Alcohol fuels achieve superior combustion efficiency because of their oxygen content together with high octane ratings. Yu et al. [13] investigated how the methanol affected the kerogen pyrolysis using ReaxFF molecular dynamics (MD) simulations. The study showed that methanol integration changed kerogen's thermal decomposition patterns and changed the creation of essential pyrolysis products. The collective findings from these studies demonstrate how alcohol additives can influence the hydrocarbon pyrolysis process and suggest encouraging applications for fuel optimization in energy solutions [14]. Incorporating alcohol additives into ammonia-methane blends offers enhanced combustion properties.

While alcohol additives such as ethanol and methanol have been promising to improve combustion characteristics and reduce emissions of pollutants, they are highly sensitive to fuel composition, reaction kinetics, and operating conditions in the formation of nitrogen oxides. Because of the complicated nature of the interactions involved, traditional modelling approaches are not sufficient in determining the non-linear relationship present in the NO_x

formation in ammonia–methane–alcohol systems. This has led to a greater need for tools that can handle correlations between multiple variables and make accurate predictions in a wide range of cases. Machine learning (ML) is a promising solution in this context, facilitating data-driven investigation of combustion behaviour and informing analysis derived from molecular-scale simulations [14]. With the increasing complexity of combustion systems and the need for more accurate emission prediction, ML has become a popular choice as supplementary modelling approach in combustion research. Models such as Artificial Neural Networks (ANN) have been used by researchers to accurately predict NO_x emissions, enabling real-time control of combustion parameters and effective mitigation of emissions [15]. In addition, the combination of optimisation algorithms (e.g., genetic algorithms (GA)) with ML platforms has been shown to improve operating conditions, such as temperature, pressure, and fuel–air ratio, leading to more stable and efficient combustion. By combining ANN and GA, it is possible to reduce NO_x emissions through optimising excess oxygen concentration and combustion temperature [16]. Similarly, use of ensemble models, such as Random Forest and Extreme Gradient Boosting, has gained popularity due to their robust capacity, with accuracy rates typically being over 90% in the case of gas turbines [17]. The best use of these models is in modelling non-linear and multi-dimensional relations between combustion parameters, which allows generalization over a wide range of fuel types and operating conditions [18-20]. Under the employment of feature optimization methods, their performance can be improved by reducing variable selection and conserving computational capacity. This is particularly important for real-time emission monitoring systems. As combustion systems become more intricate, there is a growing interest in hybrid approaches that combine ML algorithms with physical models, ensuring that predictions are always grounded in chemical and thermodynamic reality. Furthermore, probabilistic modelling approaches—most notably Gaussian Process Regression (GPR)—have demonstrated strong capabilities in quantifying predictive uncertainty and improving model reliability in complex flow dynamics, particularly in cold flow regimes of combustion engines [21].

The present study investigates the effects of alcohol additive substances, ethanol (C₂H₆O) and methanol (CH₄O), on the formation of NO_x in ammonia–methane combustion systems using ReaxFF MD simulations. Simulations were performed at two temperatures (2,000 K and 3,000 K) for three alcohol concentration ratios (0%, 5%, and 10%) to contrast the chemical and thermal impact of additives on NO_x emissions. To extend predictive capabilities beyond the limited scope of molecular simulations, an ML platform was used to predict NO_x formation for off-design alcohol ratios of 2%, 7%, and 12% that are beyond the original training zone. Unlike most previous ML studies, which focused primarily on interpolation within known datasets or used coarse-grained experimental data as inputs, the present work uniquely combines atomistic simulation-derived descriptors with data-driven learning to enable extrapolative predictions. This is particularly significant in the context of alcohol-blended ammonia fuels, where few studies have rarely addressed how ML models perform in extrapolation regimes, especially for non-simulated fuel compositions. Moreover, while earlier works typically use simplified or global combustion parameters, our study leverages detailed atomic-scale descriptors, such as bond energy distributions, charge dynamics, and species evolution, to inform and train ML models. Different ML models were trained and compared, including Random Forest Regression (RFR), Gradient Boosting Regression (GBR), Support Vector Regression (SVR), and Fully Connected Neural Networks (FCNN), which were experimented with different architectures and validation approaches to identify the most

suitable model for extrapolative combustion analysis. Notably, the study recommends a hybrid chemical-guided data-driven approach, whereby interpolated inputs from MD simulations are utilized to generate chemically consistent synthetic datasets. These are then used in NO_x prediction by ML without any additional high-cost MD simulations. The proposed hybrid framework is a novel, computationally efficient route to extending combustion behaviour beyond simulated conditions, promoting a reliable modelling strategy that combines atomistic scale information with scalable prediction ability for designing clean fuels.

2. Methodology

2.1. Reactive force field molecular dynamics (ReaxFF MD)

Reactive force field (ReaxFF) molecular simulations provide a robust framework for modelling chemical reactions at the atomic scale by dynamically accounting for bond formation and breaking. In contrast to traditional force fields based on fixed connectivity, ReaxFF works using bond-ordering and allows for chemical interactions to evolve in real time within highly reactive materials [22-23]. This modelling technique bridges the gap between quantum mechanical computations, which are precise but computationally difficult, and classical molecular dynamics (MD) simulations, which are effective but non-reactive. ReaxFF enables the modelling of extensive systems under extreme pressures and temperatures with a high level of precision, facilitating the physical capture of complex chemical reactions. It has been widely applied in combustion studies, offering valuable insights into reaction mechanisms, intermediate species formation, and product distributions [24]. The ReaxFF can be expressed as a function of the bond order, as described in Eq. (1). The total potential energy in ReaxFF is represented as the sum of various energy contributions, including bond energy, penalties for over- and under-coordination, lone-pair stabilization, valence and torsional angle energies, and non-bonded interactions such as Coulombic and van der Waals forces [25-26]. This formulation allows ReaxFF to accurately capture the complex interplay of bonded and non-bonded interactions in reactive systems. By parameterizing these energy terms based on quantum mechanical calculations, ReaxFF can simulate chemical processes in large systems with both computational efficiency and chemical accuracy.

$$E_{\text{system}} = E_{\text{bond}} + E_{\text{over}} + E_{\text{under}} + E_{\text{lp}} + E_{\text{angle}} + E_{\text{tors}} + E_{\text{vdW}} + E_{\text{Coul}} \quad (1)$$

2.1.1. Validation of ReaxFF

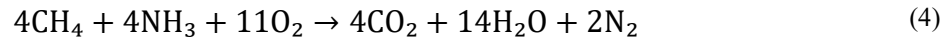
Several reactive force fields are available for the study of C/H/O/N systems, but selecting one that is both accurate and reactive for modelling NH₃/CH₄ combustion is critical. For this study, the ReaxFF force fields developed by Kulkarni et al. [27] and Zhang et al. [28] were considered, both of which have been previously validated for ammonia–hydrocarbon systems in the literature [29-30]. To assess the reliability of the selected force field in reproducing reaction energetics, calculated bond dissociation energy (BDE) values were compared with experimental and computational results. The chemical reactions governing CH₄ and NH₃ combustion involve the primary oxidation pathways of these fuels. Methane (CH₄) reacts with oxygen (O₂) to produce carbon dioxide (CO₂) and water (H₂O) as per the reaction:



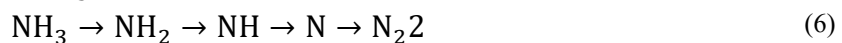
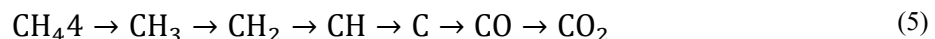
Simultaneously, ammonia (NH₃) undergoes combustion in the presence of oxygen to form nitrogen gas (N₂) and water:



In this study, a 1:1 ratio of CH₄ to NH₃ is considered, combining these two reactions into a single overall reaction:



The reaction pathways for CH₄, NH₃, and O₂ explain the formation of the primary combustion products: CO₂, H₂O, and N₂. The presence of intermediates such as CO, NH, and OH also provides critical insights into the reaction dynamics and the influence of stoichiometric ratios (λ) on the combustion process.



These intermediates are indicative of reaction progress and combustion efficiency under different stoichiometric conditions.

BDE is an important parameter for assessing the reliability of the chosen ReaxFF force field in simulating the reactivity and stability of CH₄ and NH₃. It is the accurate calculation of the bond dissociation energy and bond order (*BO*) that determines the stability and reactivity of molecules in combustion systems. BDE provides a quantitative estimate of the amount of energy required to deform a given chemical bond, and this is one of the most important parameters for calculating reaction energetics. The ReaxFF framework calculates bond energy (*E*) as a function of the bond order (*BO*), which represents the degree of bonding between two atoms [26, 31].

$$E = -D_e \cdot \text{BO} \cdot \exp(p_{be2} \cdot (1 - \text{BO}^{p_{be1}})) \quad (8)$$

$$\text{BO} = \exp\left(p_{bo1} \left(1 - \left(\frac{r}{r_0}\right)^{p_{bo2}}\right)\right) \quad (9)$$

The parameters *pbo1* and *pbo2* control how bond order decays with bond stretching or compression relative to a reference bond length r_0 . The parameters *pbe1* and *pbe2* control how bond energy depends on bond order. *De* represents the dissociation energy for the bond. This equation ensures that energy scales with bond order, reflecting the bond's contribution to the system's total energy. In this study, the bond dissociation energy (BDE) values for CH₄ and NH₃ were calculated using the ReaxFF 2009 force field developed by Zhang et al. [28] and were compared against both experimental data [32–33] and simulation results from Xu et al. [29], which used the ReaxFF 2012 force field by Kulkarni et al. [27]. For CH₄, the BDE obtained in the present study was 104.35 kcal/mol, compared to 105.0 kcal/mol in Xu et al. [29] and 102.6 kcal/mol experimentally. This results in an absolute error of 0.65 kcal/mol versus Xu et al. and 1.75 kcal/mol versus the experimental reference. For NH₃, the present study yielded a BDE of 106.09 kcal/mol, while Xu et al. reported 107.4 kcal/mol and the experimental value was 103.6 kcal/mol. This corresponds to absolute errors of 1.31 kcal/mol

and 2.49 kcal/mol, respectively. These results indicate that the ReaxFF 2009 force field produces BDE values in close agreement with both experimental benchmarks and previously published simulations, supporting its suitability for accurately capturing bond-breaking energetics in ammonia–methane combustion systems. The near equivalence of CH_4 and NH_3 BDE values also aligns with their similar molecular stabilities, as reflected in their comparable consumption rates during combustion. This supports the applicability of the ReaxFF. 2009 (Zhang et al. [28]) ReaxFF force field for exploring complex reaction mechanisms and product formations in CH_4/NH_3 systems under varying conditions.

2.1.2. Cases set-up

To investigate the influence of alcohol additives on ammonia–methane combustion, ten computational cases (C1–C10) were configured. Each case employed an equivalence ratio of $\lambda = 0.7$, a moderately fuel-rich condition typical of practical combustors where perfect stoichiometry ($\lambda = 1$) is rarely achieved. Operating under fuel-rich conditions promotes the build-up of reactive intermediates and enables detailed examination of NO_x formation pathways which is the primary objective of this study. For physical consistency, the mass density was fixed at 0.34 g/cm^3 in every simulation. Although the total number of molecular remained constant at 800, the cubic domain length was adjusted case-by-case to satisfy the density constraint, ensuring that any changes in system behaviour originate solely from variations in fuel composition or temperature. The baseline mixture comprised 422 fuel molecules—methane (CH_4) and ammonia (NH_3) in a 1:1 ratio—together with 378 oxygen molecules. Alcohol co-fuels, ethanol ($\text{C}_2\text{H}_6\text{O}$) or methanol (CH_4O), were introduced by substituting 5 % or 10 % of the original $\text{CH}_4\text{-NH}_3$ base fuel while preserving the overall molecule count. Distinct C–H bond energies and oxygen contents in selected alcohols are expected to affect their radical pools and chain-branching behaviour. Each composition was evaluated at 2000 K and 3000 K to capture temperature-dependent kinetics.

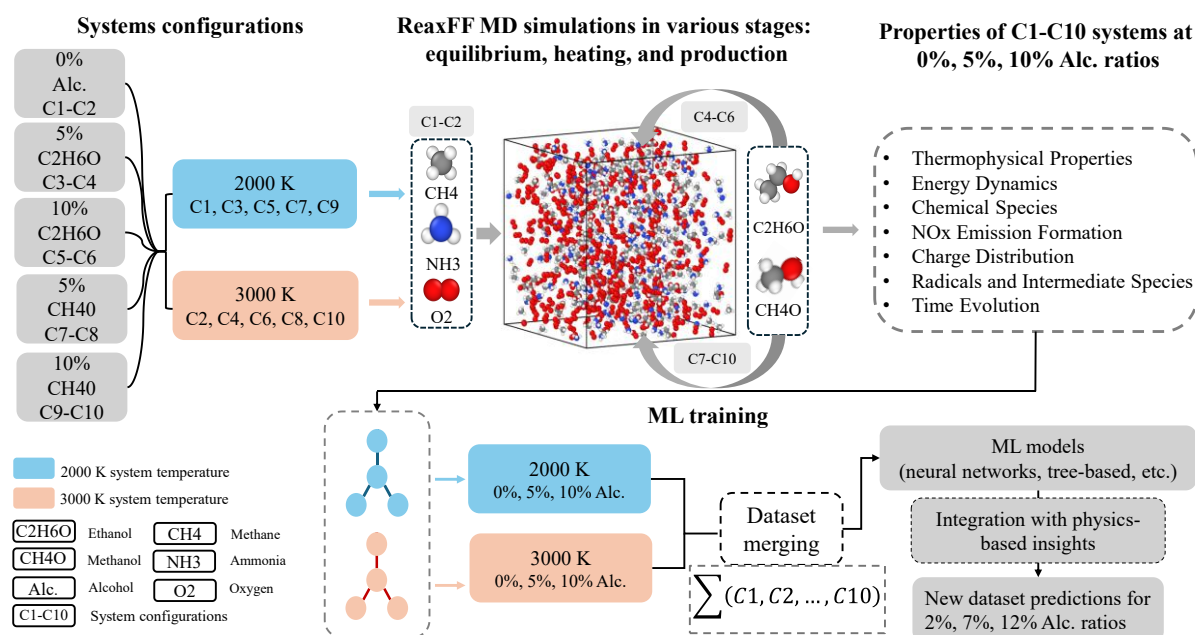


Fig. 1. Schematic representation of case configurations, fuel compositions, and simulation workflow for ammonia–methane combustion systems with alcohol additives. The diagram outlines the formulation of ten cases (C1–C10) at 2000 K and 3000 K with varying alcohol ratios (0%, 5%, 10%), molecular substitutions, and subsequent integration into a merged dataset for machine learning prediction.

Tables S1 and S2 in SI material list the full set of simulation parameters, including density, temperature, molecular composition, and corresponding cube size for every case. These data establish a consistent framework for quantifying how incremental alcohol addition modulates intermediate-species production and, ultimately, NO_x emissions under fuel-rich combustion. A visual summary of the case configurations is presented in Fig. 1, which outlines the temperature–composition matrix, the fuel replacement scheme, and the corresponding simulation domains. The diagram also highlights how the individual systems were integrated into a single dataset, later used for machine learning predictions targeting off-design alcohol ratios.

2.1.3. Simulation set-up

MD simulations were conducted using LAMMPS (Large-scale Atomic/Molecular Massively Parallel Simulator) [34], a widely used molecular dynamics platform that supports both reactive and non-reactive force fields, including ReaxFF for chemical reaction modelling. Simulations were executed on a multi-core compute node to achieve sufficient statistical sampling within a feasible wall-clock time. Initial configurations were assembled in PACKMOL [35], ensuring uniform spatial distribution, randomised molecular orientation, and avoiding initial molecular overlaps. Reactive interactions were described with the ReaxFF potential; the C/H/N/O parameterisation of Zhang et al. [28] was chosen because it reliably reproduces ammonia–methane chemistry and the associated NO_x forming intermediates.

Charge equilibration was carried out using the qeq/reax method at every timestep, and a bond order cutoff of 0.3 was used to detect significant chemical interactions [29, 30]. The simulation workflow comprised three key stages: equilibration, heating, and production. After geometrical relaxation, the system was equilibrated for 100ps in the NVT ensemble at 300 K with a 0.1 fs timestep. The temperature was then raised linearly from 300 K to the target value—either 2000 K or 3000 K—at 20 K.ps⁻¹; during this ramp, the timestep was reduced to 0.05 fs to accommodate increased atomic velocities. The main production run was performed for 500 ps at the target temperature, employing a 0.01 fs step length to resolve high-frequency vibrational modes and reactive collisions accurately [49, 50]. All dynamic stages retained the NVT ensemble to maintain constant temperature-volume conditions [29, 30, 48]. Trajectory data were analysed with the REAXC package embedded in LAMMPS to monitor reaction pathways and bond-network evolution. Post-processing was carried out with ChemTraYzer [36] supplemented by in-house Python scripts, enabling automatic species identification, pathway analysis, and quantitative evaluation of NO_x formation. Atomistic trajectories were visualised with OVITO [37] to facilitate qualitative inspection of structural changes.

2.2. Machine learning framework

2.2.1. Data structure and preprocessing

Fig. 2 shows the data processing pipeline that links MD simulations to ML models applied in this paper. ReaxFF-based MD simulations created the baseline dataset from simulations performed at temperatures 2,000 K and 3,000 K for 10 chemical cases, which are labelled C1

to C10. Each case simulated a 500ps reactive trajectory and produced a series of thermochemical and molecular descriptors, which were designed to characterise the evolving behaviour of ammonia–methane–alcohol mixtures. The resulting dataset includes 26 input features (X), encompassing key thermophysical observables such as temperature, pressure, and density, as well as energy terms including total, kinetic, and potential energies. In addition, features derived from the ReaxFF were included to represent mechanistic quantities of the direct chemical relevance. These consist of individual energy contributions: v_{ea} (atomic), v_{eb} (bond), v_{elp} (lone pair), v_{ev} (valence angle), v_{epen} (penalty), v_{ecoa} (conjugation), v_{ehb} (hydrogen bond), v_{et} (torsion), v_{eco} (conjugated), v_{ew} (van der Waals), v_{ep} (Coulomb), and v_{eqeq} (charge equilibration). Element-specific charge distribution properties were also computed: v_{qC} , v_{qH} , v_{qN} , and v_{qO} , representing the mean partial charge for each atom type, which are essential for capturing electron redistribution during combustion. Chemical identity was represented by the mass fraction of alcohol feature, which distinguishes 0%, 5%, and 10% mixed fuels, and binary indicators for ethanol and methanol, to account for molecular structure effects. These enable the models to learn not only compositional trends but also the functional impact of hydroxyl content and C–H/O–H bond energetics on various alcohol additives. A rigorous data cleaning step was employed prior to training the models. This included the detection and removal of anomalous entries owing to rare bond breakage events, unphysical charge spikes, and species mislabelling during dynamic equilibration. Outliers were eliminated using interquartile-based cutoff values, and no missing values were encountered, as molecular dynamics simulations deterministically generate complete trajectories with time-resolved data for all atoms and properties. Preprocessing was followed by 80:20 (e.g., 80% of data used for training and 20% for validation) stratified train-test splitting in a manner that ensured proportional representation of all the compositions and temperatures within the training and testing sets [14, 38].

This balance was critical to support downstream generalisation, especially in light of the hybrid extrapolation framework, which is introduced later. As illustrated in Fig. 2, the data served as input to four different ML architectures, e.g., Random Forest Regression (RFR), Gradient Boosting Regression (GBR), Support Vector Regression (SVR), and a Fully Connected Neural Network (FCNN). The NO_x output (Y) was predicted both within the training range (0%, 5%, 10%) and extrapolated beyond (e.g., 2%, 7%, 12%) using a post-processing formulation grounded in chemical trends. To determine nitrogen oxide emissions from each system, the mole fractions of individual NO_x -related species (NO , NO_2 , N_2O , and HNO_3) were extracted from the LAMMPS ReaxFF simulation outputs using the `fix reax/c/species` command. These species were tracked over time, and their aggregate concentrations were used to estimate the total NO_x emission in parts per million (ppm). The total NO_x was computed using the following formulation:

$$NO_x = \left(\frac{\sum_{i \in NO_x \text{ species}} n_i}{N_{total}} \right) \times 10^6 \quad (10)$$

Where n_i represents the number of molecules of each NO_x species (i.e., NO , NO_2 , N_2O , HNO_3) identified in the system, N_{total} is the total number of molecules in the simulation box. This equation follows standard post-processing protocols for ReaxFF molecular dynamics simulations used in combustion and pollutant analysis [23-24]. The multiplication by 106 converts the molar ratio into a ppm-scale value for better interpretability and alignment with experimental conventions.

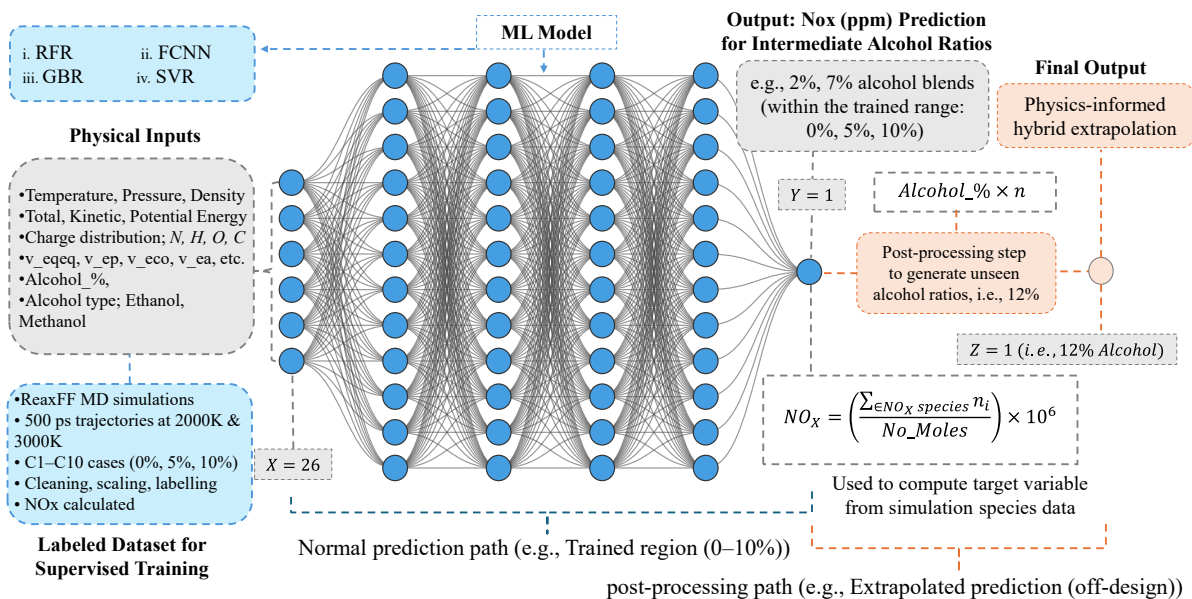


Fig. 2. Machine learning (ML) workflow integrating chemical-guided extrapolation for NO_x prediction from ReaxFF-derived combustion data. NO_x was calculated based on the normalized counts of NO_x-related species (i.e., NO, NO₂, N₂O), as described in Eq. (10)

2.2.2. ML algorithms

Four ML algorithms were chosen in this work to model the intricate interaction between combustion descriptors and NO_x emissions: RFR, GBR, FCNN, and SVR. Their capacity to capture non-linear dependencies, resilience against overfitting and proven success in thermochemical prediction tasks guided selection of these models. All the algorithms have different strengths that are well-suited to the nature of combustion-related data. RFR, as an ensemble decision tree, performs exceptionally well with high-dimensional data and produces variable importance information, which is critical in understanding the influence of physical parameters. GBR augments the same by incorporating gradient-based optimization in the construction of trees and thereby is well suited to pick up weak interactions in noisy or structured data. FCNNs, on the other hand, are capable of learning intricate, continuous functions due to their hierarchical representation power, particularly useful in tracking multi-variable chemistries' dynamics. SVR becomes a standard regression benchmark because it excels with non-linear data by using the kernel-based similarity functions to capture non-linearity. Four distinct versions of each algorithm were created to explore the effect of design choices on their performance by adjusting internal parameters. To evaluate the robustness and generalizability of tree-based algorithms (i. e., RFR, GBR), a systematic approach was taken to adjust both tree count and depth parameters. Neural networks (NN) configurations included various hidden layer counts and neuron distributions ranging from basic one or two layered networks to deep structures with up to five hidden layers. SVR configurations were altered by experimenting with different kernel functions (linear, polynomial, or radial basis) and regularisation parameters.

Table 1 summarises the architectural configurations used across all models. This systematic variation allows a comprehensive evaluation of how model complexity and hyperparameter tuning influence the prediction accuracy in a reactive system. By comparing models not only across algorithm types but also across architectures, the present study aims to determine which

models are most effective at extracting meaningful chemical reactions from ReaxFF-generated data and generalising to unobserved alcohol ratios in a chemical-guided extrapolation setting.

Table 1 Summary of hyperparameter variations and architectures for Random Forest Regression (RFR), Gradient Boosting Regression (GBR), Fully Connected Neural Network (FCNN), and Support Vector Regression (SVR) models in predicting NOx emissions.

FCNN Model Configurations														
Model	Search Method	Models Compared	NN Shape				Activation	Dropout	Batch Size	Training Steps	CV Strategy	Folds	Scoring	
FCNN 1	-	-	[100, 100]				ReLU	0.05	64	1000	K-Fold	5	RMSE	
FCNN 2	Randomised	50	[128, 128, 128, 128, 128]				Swish	0.05	128	1000	K-Fold	5	RMSE	
FCNN 3	Randomised	50	[64, 64, 64]				ReLU	0.1	32	1000	K-Fold	5	RMSE	
FCNN 4	Randomised	50	[256, 256, 256, 256, 256]				Swish	0.05	256	1500	K-Fold	5	RMSE	
RFR Model Configurations														
Model	Search Method	Models Compared	Number of Estimators	Max. Depth	Min. Split Samples	Min. Leaf Samples	Grid Estimators	Grid Max. Depth	Grid Min. Split	Grid Min. Leaf	CV Strategy	Folds	Scoring	
RFR 1	-	-	100	None	2	1	None	None	None	None	K-Fold	5	RMSE	
RFR 2	Randomised	20	600	20	2	2	[700,300,400,500,600]	12,15,18,20	2,4,8,16	2,4,8,16	K-Fold	5	RMSE	
RFR 3	Randomised	50	400	20	4	2	[200,300,400,500,600]	12,15,18,20	2,4,8,16	2,4,8,16	K-Fold	5	RMSE	
RFR 4	Randomised	30	300	20	16	2	[100,200,300,400,500]	10,20	2,4,8,16,32	2,4,8,16,32	K-Fold	5	RMSE	
SVR Model Configurations														
Model	Search Method	Models Compared	Kernel	Regularisation Parameter (C)	Kernel Coefficient (Gamma)	Grid (C)		Grid (Gamma)		CV Strategy	Folds	Scoring		
SVR 1	-	-	RBF	1	Scale	None		None		K-Fold	5	RMSE		
SVR 2	Randomised	10	RBF	100	Scale	[0.1, 1, 10, 100, 1000]		scale, 0.01, 0.1		K-Fold	5	RMSE		
SVR 3	Randomised	20	RBF	100	Scale	[0.001, 0.01, 0.1, 1, 10, 100]		scale, auto, 0.0001, 0.01, 0.1		K-Fold	5	RMSE		
SVR 4	Randomised	20	Polynomial	1000	0.1	1000		scale, 0.01, 0.1		K-Fold	5	RMSE		
GBR Model Configurations														
Model	Search Method	Optimised Parameters	Number of Estimators	Learning Rate	Max. Depth	Min. Split Samples	Min. Leaf Samples	Subsample	Grid Max. Depth	Grid Min. Split	Grid Min. Leaf	CV Strategy	Folds	Scoring
GBR 1	-	No	500	0.05	6	2	1	1	None	None	None	K-Fold	5	RMSE
GBR 2	Grid Search	Yes	300	0.01	8	8	4	1	3	5	4	K-Fold	5	RMSE
GBR 3	Grid Search	Yes	800	0.03	6	4	4	1	10	10	6	K-Fold	5	RMSE

2.2.3. Model evaluation

Performance comparison of different ML models employed mean absolute error (MAE), mean squared error (MSE), Pearson correlation coefficient (PCC), and coefficient of determination (R^2) as regression evaluation metrics. MAE calculates the average error magnitude while MSE determines the average error dispersion with MSE being more affected by outliers than MAE [39–40]. PCC and R^2 represent the correlation between predicted results and actual data points using their correlation measurement [41–42]. All the models were trained using 80% of the data to keep the remaining 20% as a test set for a fair comparison and generalization [38]. The analysis of the absolute error values and correlation metrics of the training and test sets can be used to identify overfitting and to choose the best model to interpret physical and chemical principles.

2.3. Chemical-guided extrapolation

To extend the predictive capability of different ML models beyond the training range, a chemical-guided extrapolation strategy was employed. This approach aimed to infer NOx emissions for untrained alcohol ratios, specifically 2%, 7%, and 12%, by leveraging both data-driven models and domain-specific chemical insights derived from ReaxFF simulations. As illustrated on the right panel of Fig. 2, the post-processing workflow builds upon the trained model’s outputs at known alcohol concentrations (0%, 5%, and 10%). The key idea was to avoid the need for new MD simulations at unseen compositions, and instead to estimate the target variables by interpolating or extrapolating trends observed in the training data. This hybridisation of ML and physical chemistry offers a practical route for off-design predictions without incurring the computational cost of generating new datasets. Specifically, for in-range predictions such as 2% and 7%, a linear interpolation scheme was adopted between the adjacent training points (e.g., 0%–5%, 5%–10%). This approach assumes smooth transitions in NOx behaviour across small alcohol increments, which was consistent with the gradual trends captured by ReaxFF simulations. For out-of-range prediction at 12%, which is a value not seen during model training, a scaling-based extrapolation technique was applied. This was informed by the observed gradient between the 5% and 10% alcohol systems and adjusted proportionally beyond the upper bound. To mathematically implement this extrapolation, a scaling coefficient is introduced and is expressed below:

$$Feature_{12\%} = Feature_{10\%} + \left(\frac{12 - 10}{10 - 5} \right) \times (Feature_{10\%} - Feature_{5\%}) \quad (11)$$

This transformation was applied independently to each input feature before feeding it through the trained models, allowing the prediction of NOx emissions for novel alcohol levels. This method is described in Fig. 2 as post-processing step to generate unseen alcohol ratios, and it bridges the gap between chemical-guided trends and data-driven modelling. The underlying rationale for this strategy is based on the smooth, thermochemically governed nature of alcohol substitution in reactive systems. Then, ML models, which were trained on clean, labelled inputs, were able to capture the nonlinear coupling between chemical features and NOx formation, reinforcing the robustness of predictions. By combining these two pillars, e.g., data-

driven learning and chemically grounded extrapolation, the hybrid method demonstrated in this study offers a reliable alternative to conventional simulation-heavy routes for combustion design. This novel approach enables fast, cost-effective insights into emission reduction under off-design conditions, showcasing a vital step towards adaptive, intelligent optimisation in combustion chemistry.

3. Results and Discussion

3.1. MD simulation results

3.1.1. Charge distribution trends

The influence of alcohol additives on charge redistribution during ammonia–methane combustion was assessed by monitoring the ReaxFF partial charges of nitrogen (N), hydrogen (H), carbon (C), and oxygen (O) atoms. Figs. 3 and 4 present the average charge–time profiles for all mixtures (0%, 5%, and 10% alcohol) at 2,000 K and 3,000 K, respectively. At 2,000 K in Figs. 3(a–d), the nitrogen sites acquire progressively more positive charge in every mixture, the rise being most pronounced for the methanol-containing cases C7 and C9. Enhanced electron withdrawal from nitrogen in these systems points to an alcohol-assisted oxidation route for NH_3 , which is consistent with the hydroxyl-rich environment created by methanol. Hydrogen, by contrast, maintains an almost constant charge, with only minor increases observed at higher alcohol ratios; this stability suggests a passive role for H atoms during the early radical-initiation period. Carbon behaviour depended strongly on additive type and ratio. The reference mixture C1 (0% alcohol) retained the most negative carbon charge throughout, whereas the richer ethanol and methanol blends (C5 and C9) drifted gradually toward neutrality. The shift is attributed to the greater oxygen content of alcohols, which pulls electron density away from carbon as additional C–O bonds form. A parallel trend emerged for oxygen: in all alcohol-rich mixtures, the O atoms became steadily more negative, reflecting growth of partially reduced species, principally OH groups and nascent NO_x intermediates.

At the elevated temperature of 3,000 K in Figs. 4(a–d), the partial charge dynamics evolve significantly. Throughout the run, the net charge on nitrogen declines and in case C6, becomes slightly negative, indicating very rapid ammonia dissociation and prompt conversion toward nitric oxide. Hydrogen partial charge rises in every mixture, most clearly in the alcohol-rich systems, illustrating a pattern that reflects faster hydrogen-abstraction reactions and elevates OH and H radical production. C atoms exhibit a general trend toward increased positivity (see Fig. 4(c)), showing the steepest climb in C10. This behaviour supports the idea that high thermal energy promotes extensive carbon oxidation, especially in methanol-enriched mixtures. Oxygen again becomes more negative and more quickly than that at 2,000 K, confirming that the 3,000 K environment is substantially more reactive.

Collectively, these temperature-dependent charge shifts underscore the delicate balance between the fuel composition and radical chemistry. Methanol, in particular, intensifies electron redistribution, which is a factor that is expected to influence the subsequent NO_x -formation pathways discussed in the following section.

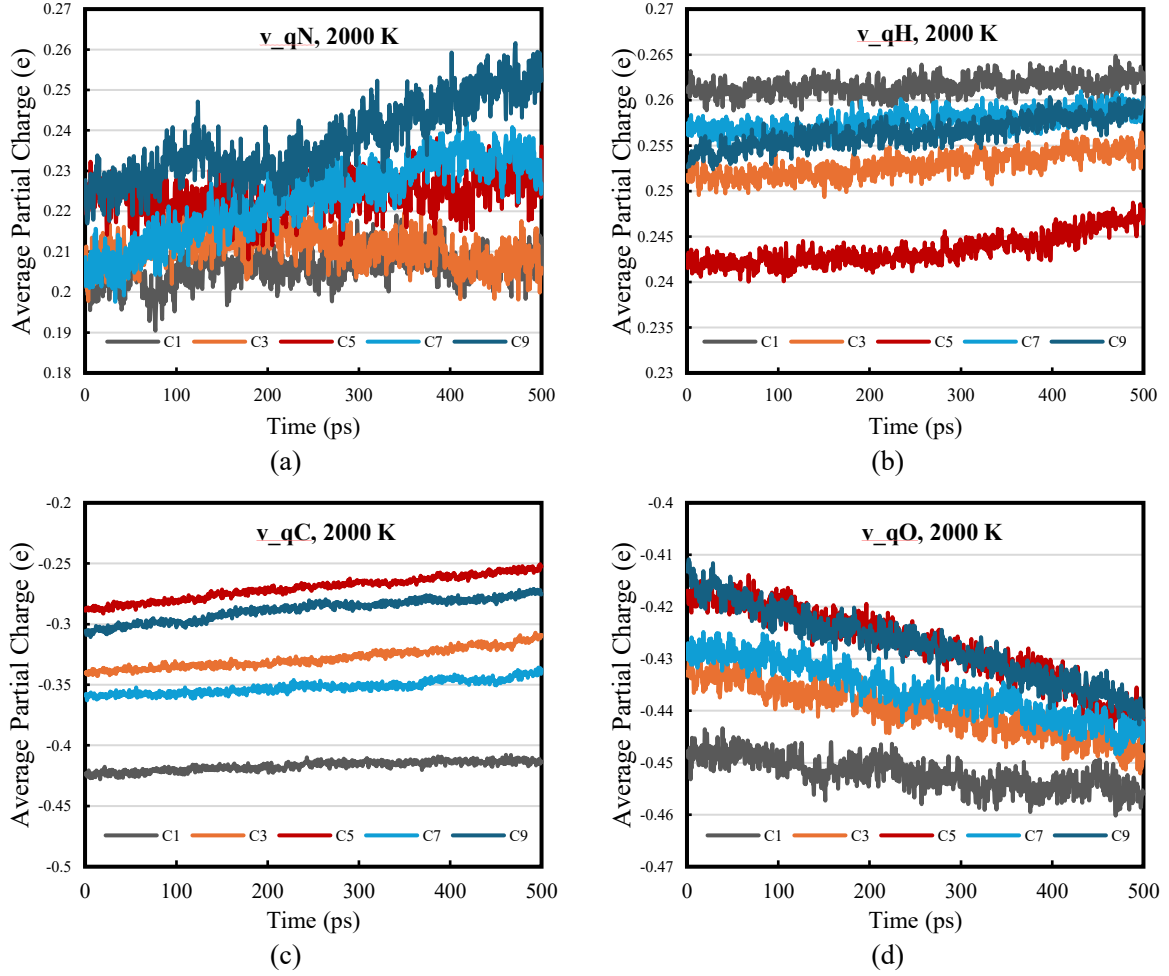
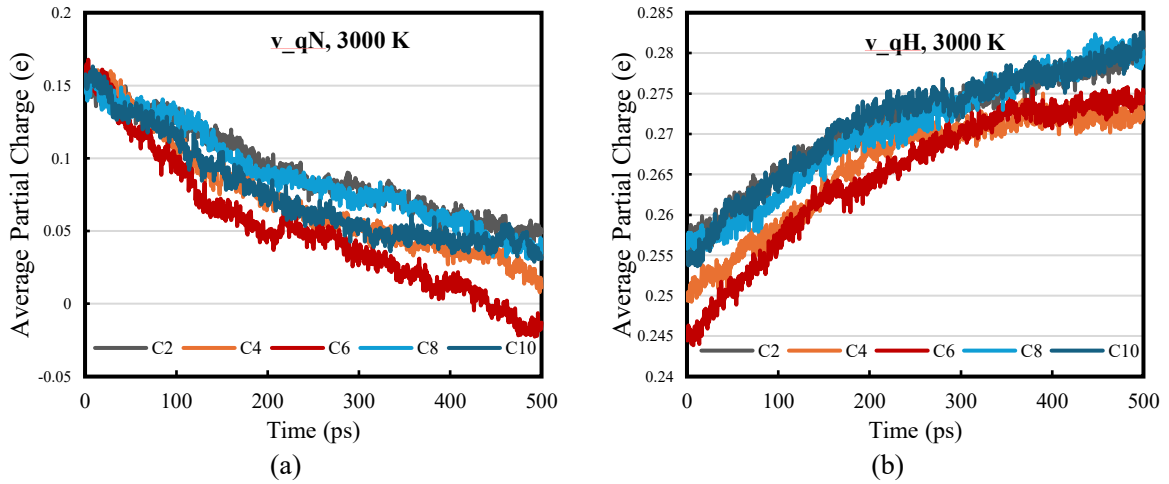


Fig. 3 Time evolution of average partial charges for nitrogen (N), hydrogen (H), carbon (C), and oxygen (O) atoms at 2,000 K across C1, C3, C5, C7, C9 cases: (a) v_qN ; (b) v_qH ; (c) v_qC ; and (d) v_qO .



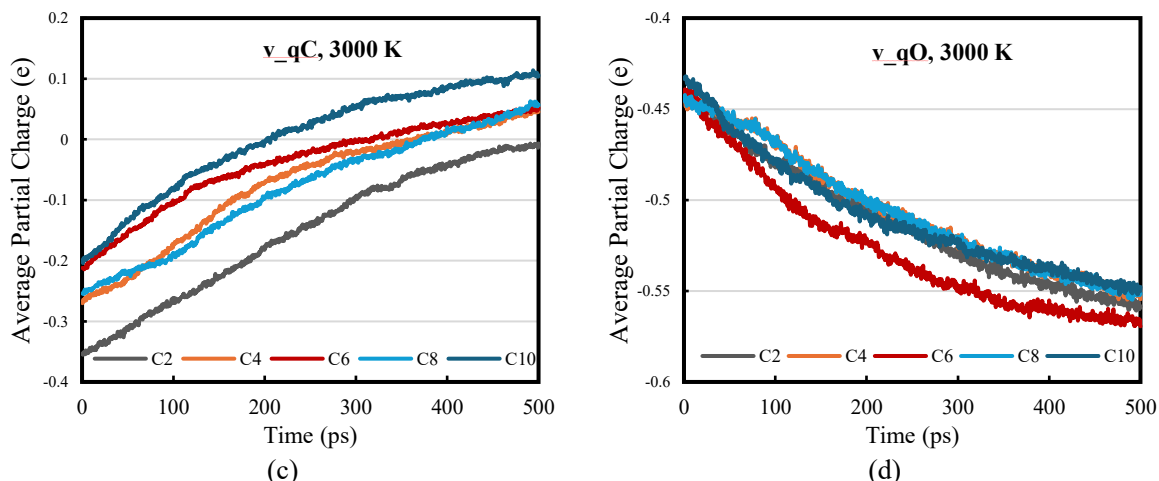


Fig. 4 Time evolution of average partial charges for nitrogen, hydrogen (H), carbon (C), and oxygen (O) atoms at 3,000 K across C2, C4, C6, C8, C10 cases: (a) v_{qN} ; (b) v_{qH} ; (c) v_{qC} ; and (d) v_{qO} .

3.1.2. Charge equilibration and NO_x emissions

Charge equilibration energy in ReaxFF simulations reveals the electron redistribution during chemical processes. Fig. 8 displays how this parameter changes during combustion at 2,000 K (see Fig. 5(a)) and 3,000 K (see Fig. 5(b)), highlighting the role of alcohol additives in forming dynamic electronic structures.

During the simulation at 2,000 K, mixtures that contain methanol show significantly lower charge equilibration energies when compared with other mixtures. The system demonstrates a more stable electron distribution, which can be primarily attributed to the larger number of electronegative oxygen atoms present in alcohol molecules. The single C atom and pronounced polarity of methanol lead to early polar interactions that accelerate the electron delocalisation and subsequently decrease the excessive charge build-up on reactive intermediates [43]. The base fuel (C1, 0% Alc.) demonstrated the maximum equilibration energy, suggesting a less favourable charge distribution and probably slower radical reactions. The influence of alcohol additives becomes even more pronounced at 3,000 K (see Fig. 5b). At this elevated temperature, ethanol-containing mixtures, particularly C6 (10% ethanol), achieved the maximum equilibration energy among all cases, underscoring their high reactivity and delayed stabilisation of the charge network. Conversely, methanol-rich systems, such as C10, show more moderate equilibration trends, indicating a superior capacity for sustaining intermediate species without excessive charge localisation. The increased thermal energy in these cases amplifies polar bond interactions to accelerate charge redistribution processes, especially in oxygen-rich molecular environments.

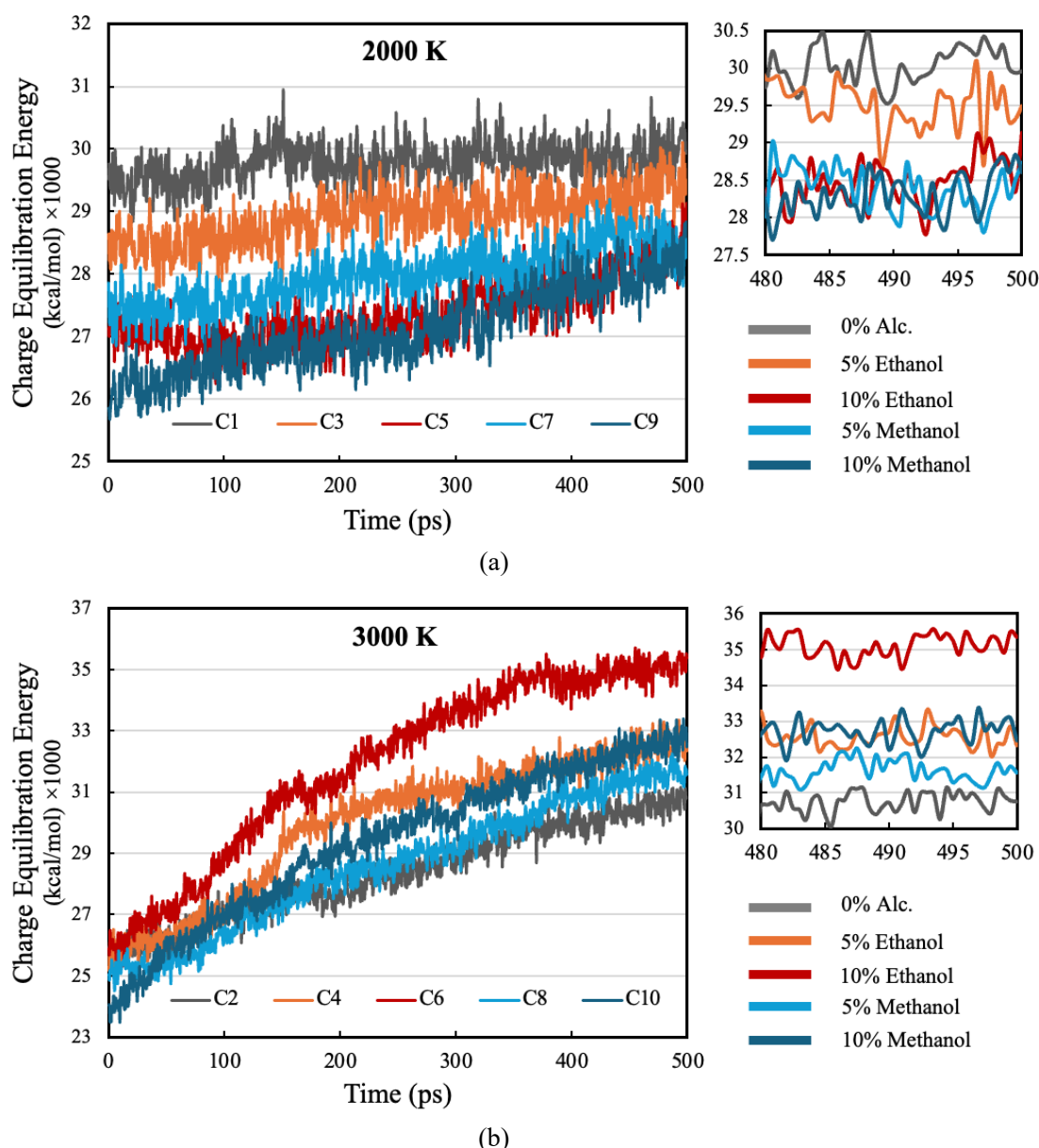
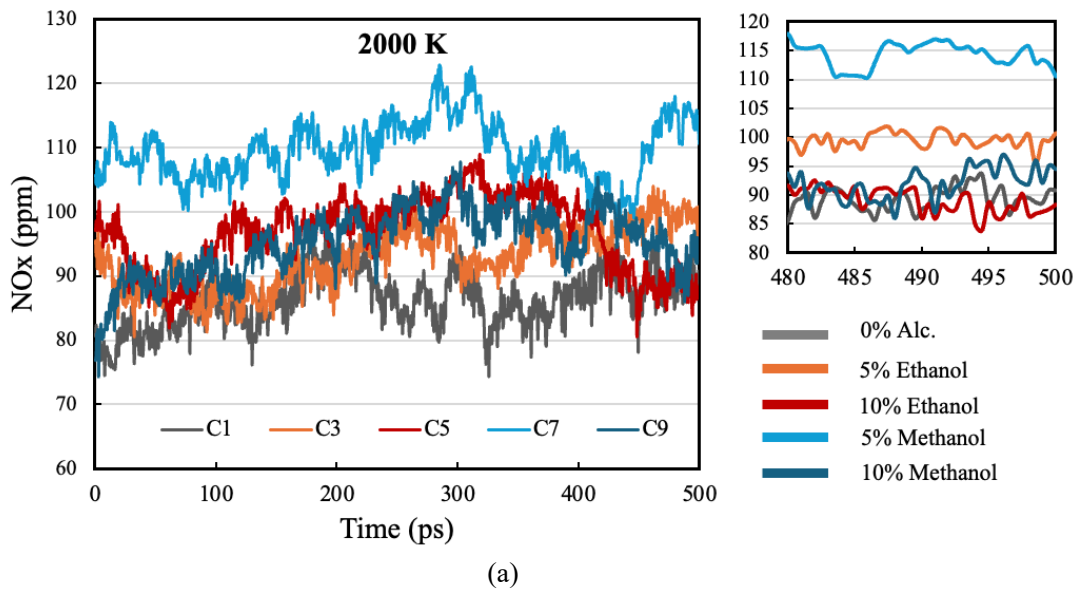


Fig. 5 Temporal evolution of charge equilibration energy for all fuel blends (0%, 5%, 10% Alc.) at: (a) 2,000 K and (b) 3,000 K. Insets magnify the final 20ps to highlight the equilibrium behaviour.

A direct connection can be observed between charge equilibration dynamics and NO_x formation trends, as displayed in Fig. 6. At 2,000 K in Fig. 6(a), NO_x emissions are highest in methanol-containing blends, particularly C7 (5%) and C9 (10%), corresponding closely to the steepest charge gradient observed in those mixtures. The connection between electron-rich conditions caused by polar additives and early NO formation demonstrates that rapid NH₃ oxidation drives this process [44]. At 500ps, the base fuel C1 produces a NO_x level of 90.79ppm; conversely, C5 including 10% ethanol obtains the lowest NO_x concentration at 88.31ppm. At 100.76ppm and 110.54ppm respectively, C3 with 5% ethanol and C7 with 5% methanol produce higher NO_x emissions; C9 with 10% methanol produces 94.46ppm. Using 10% methanol in fuel results in lower NO_x emissions compared with the base fuel although NO_x emissions rise with other alcohol additives. At 3,000 K in Fig. 6(b), however, the NO_x profiles reverse. The blend with the highest ethanol content demonstrates minimal NO_x output, illustrating a change in dominant chemical reaction routes. Here, the faster oxidation kinetics

enabled by high temperature and coupled with the stabilising characteristic of ethanol's molecular structure, appear to suppress NO formation. Methanol-containing mixtures, on the other hand, remain more reactive over time, with higher NO_x levels sustained at the final 20ps (see inset in Fig. 6(b)). The base fuel (C2) produces 109.95ppm of NO_x at 500ps while C6 with 10% ethanol results in the lowest NO_x level at 66.46ppm, which is followed by C10 with 10% methanol at 76.84ppm, then C4 containing 5% ethanol at 81.63ppm, and C8 with 5% methanol at 89.99ppm. Methanol promotes NO_x formation via enhanced reactivity and rapid oxygen donation, primarily through NO₂ and HNO₃ intermediates. In addition, alcohol-derived radicals such as OH become more active at high temperatures to interact with nitrogen-containing intermediates, thereby stopping the forming routes of NO_x [46-47]. NO_x concentration inversions caused by variations in temperatures demonstrate how various alcohol types and concentrations affect this phenomenon. Methanol leads to early NO_x production when the temperature is moderate. However, ethanol reduces NO_x output at high temperatures even though it contains more energy. At 3,000 K, 10% ethanol reduces NO_x emissions by approximately 39.5% compared to the base fuel, while 10% methanol achieves a 30.1% reduction. These findings underscore ethanol's superior role in suppressing NO_x at high temperatures. It can be concluded that alcohol additives, particularly ethanol, emerge as promising solution for cleaner combustion by lowering emissions while supporting thermal efficiency improvements. This transition in NO_x trends from 2,000 K to 3,000 K reflects a fundamental shift in dominant chemical mechanisms.



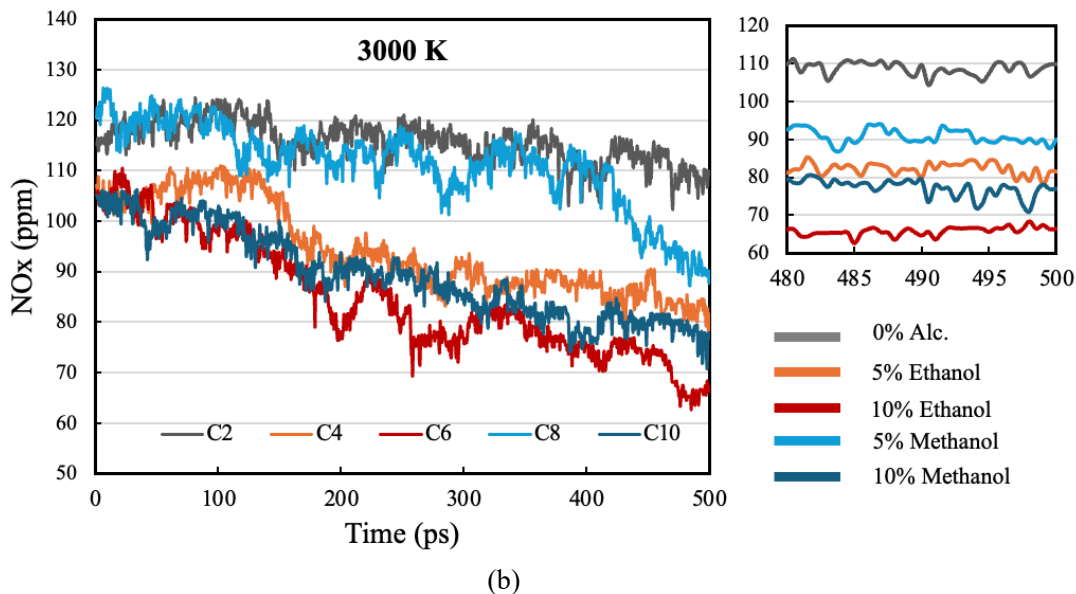


Fig. 6. NO_x emissions over time for: (a) 2,000 K and (b) 3,000 K cases. Trends are directly linked to alcohol type (ethanol and methanol) and concentration (0%, 5%, 10% Alc.). Insets show stabilisation levels at the final 20ps of the simulation.

3.1.3. Dominant reaction pathway

To elucidate how alcohol additives modulate nitrogen–oxygen reaction networks during combustion, Table 2 compiles the forward and reverse frequencies of the most active NO_x-associated reactions across all ten fuel systems (C1–C10). The reactions were identified based on their participation in NO, NO₂, HNO, HNO₂, and HNO₃ interconversion loops, critical mechanisms governing NO_x formation and removal. As observed, the base case (C1, 2000 K) exhibits strong engagement of NO₂ ⇌ HNO₃ and HNO₃-related formation pathways, reflecting the dominance of higher-order nitrogen oxides under lower-temperature oxidative conditions. At 3000 K (C2), the reaction network shifts toward simpler cycles such as HNO₂ ⇌ NO and NO ⇌ HNO, indicating increased fragmentation of NO_x species and reduced stability of nitric acid derivatives at elevated temperatures. The addition of alcohols introduces pronounced shifts in pathway dominance and reversibility. Ethanol-blended systems (C3, C5, C4, C6) continue to feature NO₂–HNO₃ cycling, particularly at 2000 K, where NO₂ ⇌ HNO₃ remains among the top reversible pathways. This suggests ethanol's role in temporarily stabilizing NO₂ into higher-order oxides like HNO₃, a phenomenon that contributes to reduced free NO concentrations. At 3000 K, ethanol-enhanced systems (notably C6) show elevated activity in NO ⇌ HNO₂ and HNO₂ ⇌ NO+NO reactions, reinforcing the interpretation that ethanol increases cycling efficiency within intermediate species, thus delaying direct NO buildup.

In contrast, methanol-enriched systems (C7, C9 at 2000 K and C8, C10 at 3000 K) reveal a marked shift in reaction priorities. The most frequent reactions are centred on NO ⇌ HNO and NO ⇌ HNO₂, with strong reverse reaction rates that exceed or match forward activity. This indicates methanol's robust effect in diverting reactive nitrogen intermediates away from NO₂ production. Notably, in C10, the NO ⇌ HNO₂ reverse flux reaches 46, among the highest of all cases, highlighting methanol's superior capacity to suppress NO₂ accumulation via intermediate stabilization. These trends are consistent with methanol's high oxygen content and rapid radical propagation, which facilitate hydrogen transfer reactions that reduce NO directly to inert or less reactive species.

The results presented in Table 2 demonstrate that both ethanol and methanol additives effectively reconfigure the NO_x reaction pathways, albeit via distinct chemical routes. Ethanol fosters temporary sequestration of NO₂ into HNO₃ under mild conditions and supports rapid NO–NO₂ cycling under high temperatures. Methanol, by contrast, emphasizes intermediate suppression and pathway deflection, preventing NO from converting into NO₂ or higher-order NO_x species.

Table 2. Dominant NO_x reaction pathways and their forward and reverse frequencies across C1–C10 fuel systems.

Reaction	Systems	Forward Reaction Frequency									
		C1	C2	C3	C4	C5	C6	C7	C8	C9	C10
NO ₂ ⇌ HNO ₃		64	0	50	0	52	0	52	0	58	0
NO ⇌ HNO		0	0	0	36	0	42	0	42	0	28
NO ⇌ HNO ₂		0	27	0	9	8	42	0	36	0	48
NO ₂ ⇌ NO		14	16	26	22	18	20	36	24	20	22
NO + NO ⇌ HNO ₂		0	20	0	16	0	0	0	39	0	24
HNO ₂ ⇌ NO		0	21	6	0	0	0	14	0	12	0
HNO ₃ ⇌ NO ₂		0	0	0	0	18	0	0	0	0	0
NO ⇌ N#N		0	6	0	8	0	10	0	9	0	4
HNO ₂ + HNO ⇌ NO + NO		0	0	0	0	0	12	0	16	0	20
		Reverse Reaction Frequency									
NO ₂ ⇌ HNO ₃		46	0	48	0	48	0	50	0	52	46
NO ⇌ HNO ₂		0	26	0	22	6	30	0	32	0	46
NO ⇌ HNO		0	12	0	28	0	44	0	30	0	20
NO ⇌ NO ₂		12	14	10	16	14	18	16	14	6	12
HNO ₃ ⇌ NO ₂		0	0	0	0	9	0	20	0	0	0
HNO ₂ ⇌ NO		0	15	4	0	0	36	4	0	10	0
NO ₂ +NO ⇌ HNO ₂		3	15	0	0	0	0	0	18	0	3
NO ⇌ N#N		0	2	0	6	0	6	0	0	0	4
NO ⇌ HNO ₂ +HNO		0	9	3	9	0	0	0	15	0	0
HNO ₂ +HNO ⇌ NO+NO		3	12	0	4	9	8	4	12	4	16

3.2.ML predictions

This section explores how ML models are applied to predict NO_x emissions from ammonia–methane–alcohol combustion based on previous MD simulation data. The goal is twofold: we first conduct model performance assessments with different architectures and then demonstrate the ability to make extrapolative predictions for off-design alcohol blends at 2%, 7%, and 12%. By training on simulation-derived features that characterise the charge distribution, energy dynamics, and thermophysical properties, the ML models were hoped to identify patterns in NO_x behaviour without running additional computationally expensive MD simulations. Four

algorithms were considered in the predictions, including RFR, GBR, SVR, and FCNN, along with four distinct architectural configurations in each model. The comparison of predictions between these models allows for a deeper understanding of how algorithm design affects the predictive accuracy, stability, and feature sensitivity.

3.2.1. Model performance evaluation

The training process utilized 80% of the data while the test set contained the remaining 20%. The evaluation process for all the models utilized five-fold cross-validation to maintain consistency across algorithms while utilizing the root mean square error (RMSE) as the primary measure of scoring performance. For each ML model, four configurations were tested, varying in depth, complexity, and key hyperparameters (e.g., number of estimators for RFR and GBR, regularisation constants for SVR, and neuron layout and dropout for FCNN). Although each algorithm followed the same cross-validation-based selection strategy, Fig. 7 presents the procedure for RFR as a representative example of how model architecture was tuned and evaluated to identify the most reliable configuration. The selection process for Random Forest models is illustrated in Fig. 7, where the performance of four architectures is benchmarked using RMSE across validation folds. The RFR2 configuration emerged as the best performer, offering the lowest error and most stable training-to-test generalisation. Similar procedures were applied to GBR, SVR, and FCNN, with their optimal architectures, e.g., GBR4, SVR1, and FCNN2, which were selected on the same basis. The superior performance of RFR2 can be attributed to its architectural depth and optimal tuning of hyperparameters such as the number of estimators (600) and controlled tree depth (maximum depth of 20), which provided a robust bias–variance balance. Unlike SVR1 and FCNN2, which struggled with the complex nonlinearities intrinsic to combustion chemistry and MD data, RFR2 benefited from ensemble averaging across numerous trees, effectively capturing the stochastic and thermochemical variability of MD-derived features. In contrast, SVR1, while demonstrating reliable performance under constrained input dimensions, failed to generalise across multi-variable interactions. Particularly when trained with larger batch sizes (128), FCNN2, which employed a deep swish-activated 5-layered architecture, performed well, suggesting its use for highly nonlinear problems with dense feature entanglement. Low learning rates and regularisation strategies helped the tree-based GBR4 to perform remarkably well. RFR2, on the other hand, confirmed its place as the best overall performer in the commotion of NO_x prediction by reconciling noise, capturing high-dimensional nonlinearity, and providing interpretable variable importances.

Quantitative comparisons for all models are summarised in Table 3, which reports the MMAE, MSE, PCC, and R² values for each configuration. Among all models, RFR delivered superior performance, showing MAE and MSE values significantly close to zero and R² and PCC measurements close to 1. SVR showed higher variance and lower accuracy because it struggled to detect complex non-linear relationships in the feature space despite GBR and FCNN presenting respectable results. The results demonstrate the effectiveness of ensemble models such as RFR when dealing with complex and interrelated features extracted from atomistic simulations. The RFR2 outperformed all the other models because it had the lowest MAE (0.661) and highest R² (0.993), indicating superior predictive capability. Strong performance from the FCNN models, as their MAE scores ranged from 1.740 to 2.036 and their R² scores peaked at 0.940, showing consistent and generally correct predictions. The GBR demonstrated moderate performance (e.g., GBR3). The SVR exhibited the lowest performance level as

shown by its high error margin ($MAE = 2.285$) and relatively poor R^2 value (0.903), indicating constrained generalization capacity. The results demonstrate RFR's strong performance capabilities and establish FCNN as a powerful substitute specifically when dealing with intricate feature interactions. The combination of their robustness with their low sensitivity to noise made these models ideal for the prediction of NO_x emissions in chemical reactions. The following discussions examine both the learning process of the four models from simulation data and their ability to predict NO_x emissions for unknown alcohol concentrations along with the physical importance of key features.

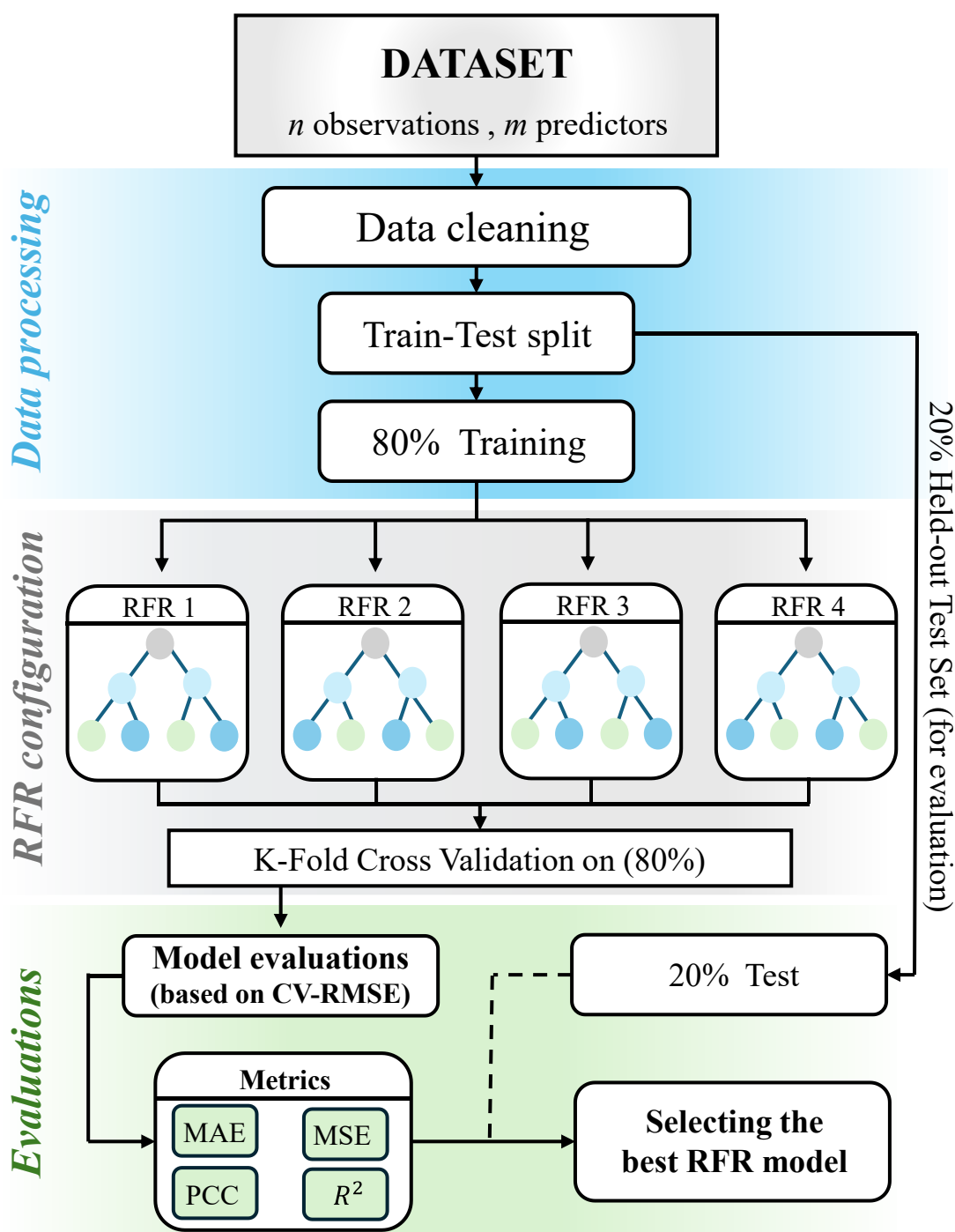


Fig. 7 Workflow of Random Forest Regression (RFR) model development including data processing, training of four configurations (RFR 1–4), and evaluation using multiple metrics to select the best-performing model.

Table 3 Model comparison of NOx (ppm) prediction between various ML models (RFR, FCNN, GBR, and SVR) in terms of evaluation metrics (MAE, MSE, PCC, and R²).

Output	Model	MAE	MSE	PCC	R ²
NOx (ppm)	FCNN 1	2.036	6.616	0.960	0.919
	FCNN 2	1.740	4.913	0.970	0.940
	FCNN 3	1.847	5.539	0.967	0.932
	FCNN 4	1.824	5.359	0.967	0.935
	GBR 1	2.299	8.394	0.947	0.897
	GBR 2	2.100	7.641	0.952	0.912
	GBR 3	1.953	7.001	0.961	0.922
	GBR 4	1.849	6.488	0.966	0.925
	RFR 1	1.012	1.715	0.990	0.983
	RFR 2	0.661	0.764	0.995	0.993
	RFR 3	0.798	1.105	0.993	0.991
	RFR 4	0.684	0.833	0.996	0.979
	SVR 1	2.285	7.941	0.951	0.903
	SVR 2	2.295	7.932	0.951	0.903
	SVR 3	2.285	7.942	0.951	0.903
	SVR 4	2.308	7.842	0.951	0.904

As shown in Fig. 8, a comparison of predicted NOx values by the best models from each ML group against the actual values has been made. The scatterplots demonstrate the correspondence between model outputs and real data (MD data) values while the dashed diagonal line indicates perfect prediction accuracy. Among all models, RFR demonstrates minimal divergence from the 1:1 line, indicating its exceptional capability to model nonlinear relationships within the combustion data. The SVR1 (Fig. 8(a)) and FCNN2 (Fig. 8(b)) show a wider dispersion that demonstrates significant prediction errors mainly at both ends of the NOx range. This pattern reinforces earlier numerical results: The tree-based RFR2 model demonstrates superior robustness in capturing feature interactions and achieves better generalization across different alcohol compositions. FCNN2 demonstrates adequate predictive capability but shows signs of overfitting or marginal case learning deficiencies due to increased scatter at elevated NOx levels. SVR1 demonstrates effective trend approximation capabilities but suffers from slight bias and reduced performance at extreme data points. These trends are consistent with the values of MAE, MSE, and R² reported in Table 3, further confirming the statistical superiority of RFR2 model.

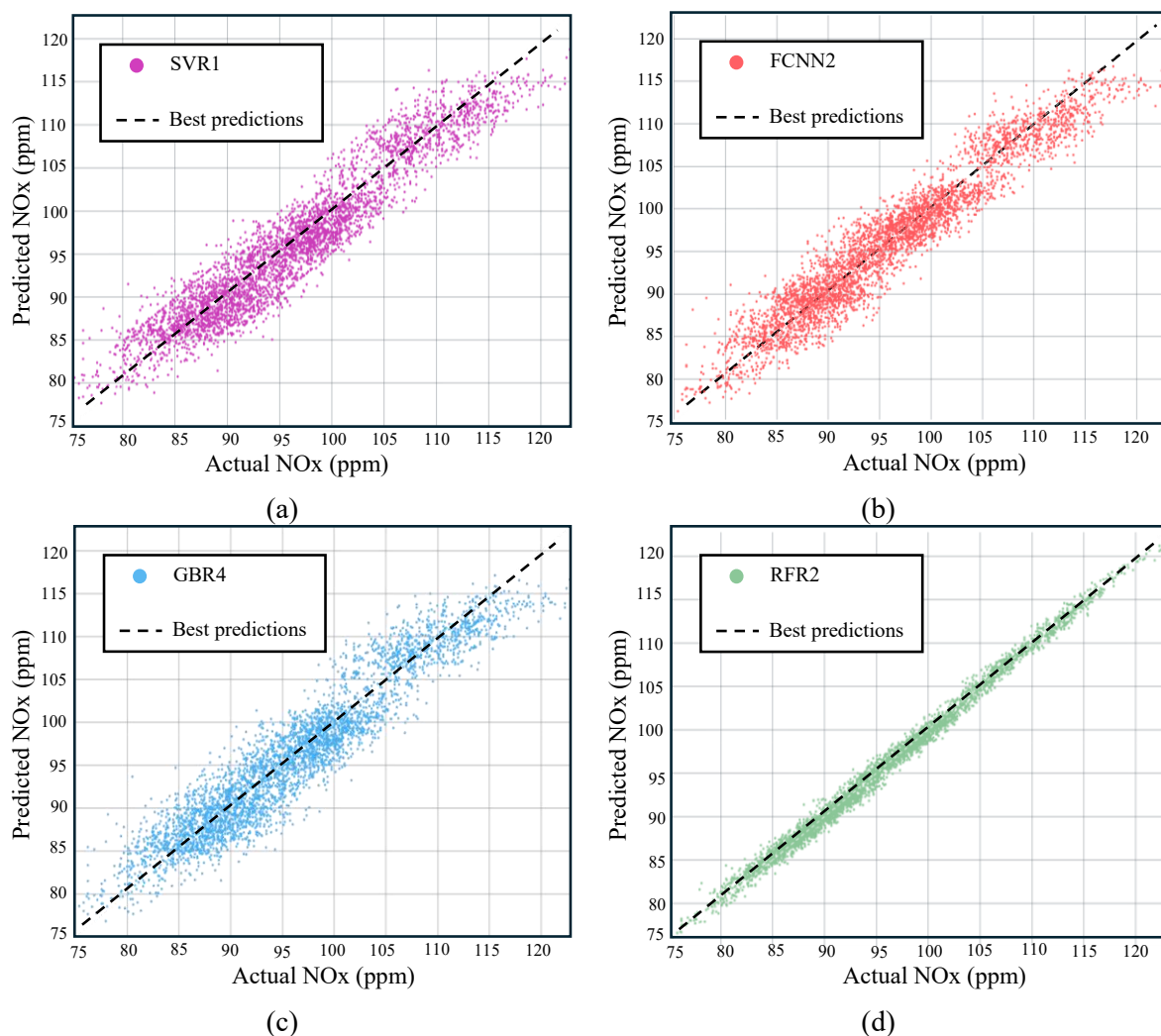


Fig. 8 Actual vs. predicted NOx (ppm) values for the best configuration of each ML model (RFR2, GBR4, SVR1, and FCNN2): (a) SVR1; (b) FCNN2; (c) GBR4; and (d) RFR2. RFR2 shows the closest match to the ideal prediction ($y = x$), indicating the best performance. SVR exhibits the highest deviation.

Turning to learning curves in Fig. 9, additional insight is gained into the stability and training behaviour of each model. RFR2 again leads with the lowest test set error and smooth convergence across iterations, indicating both reliability and minimal overfitting. Its error bars shrink progressively, showing increased confidence with additional training data. In comparison, FCNN2's learning pattern is erratic along with training error fluctuating between epochs, suggesting sensitivity to architecture or potential instability during optimisation. This behaviour is common in deep learning models when hyperparameters are not fully tuned or the dataset lacks sufficient diversity to support deeper generalisation. GBR4 and SVR1 models follow expected paths: GBR4 progresses through gradual convergence whereas SVR1 shows a significant difference between its training and test performance, hinting potential underfitting or improper regularisation. SVR1's performance gap between training and test outcomes underscores its inability to manage intricate, high-dimensional data. These plots serve not only to validate the ranking of model performance but also to visualise the chemical features behind those outcomes. Although the ensemble learning structure of RFR2 shows optimal performance with the combustion dataset, FCNN2 needs additional adjustments to achieve comparable results along with its nonlinear learning capabilities.

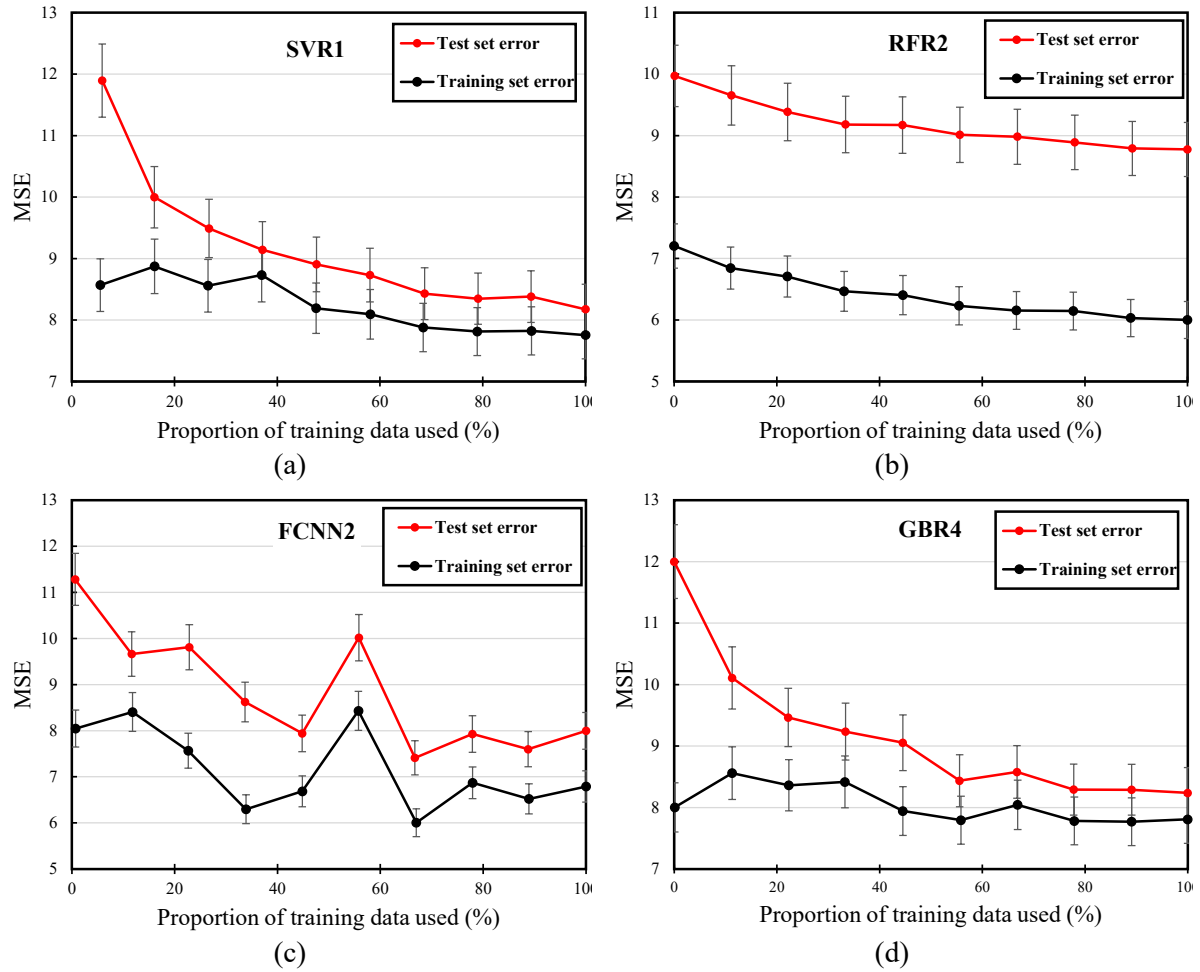


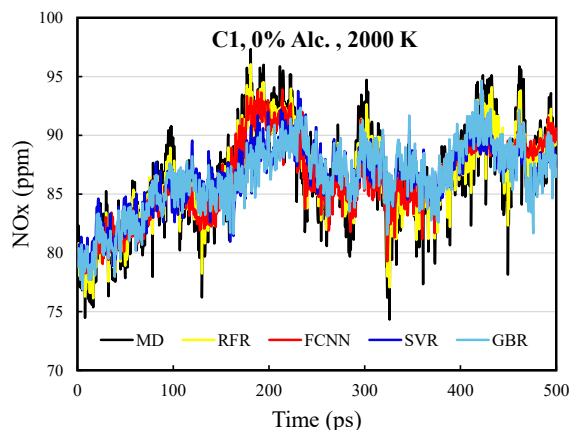
Fig. 9 Learning curves for the best-performing ML models. Plots show training and test RMSE across training epochs (FCNN) or estimators (RFR/GBR), highlighting convergence behaviour and model stability.

3.2.2. Validation of ML predictions

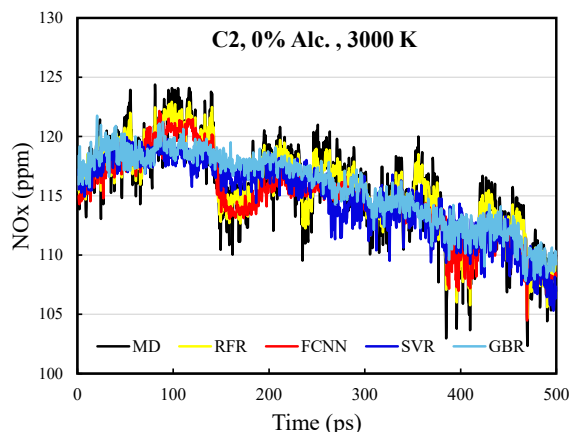
The predictive robustness of trained ML models was assessed by comparing their outputs against MD-derived NO_x values over time across ten combustion cases (C1–C10) that examined different alcohol concentrations (0%, 5%, 10%) and both ethanol and methanol blends at temperatures of 2,000 K and 3,000 K. Figs. 10 (a–j) presents the time-resolved predictions for NO_x (ppm) from four ML models, e.g., RFR (yellow), FCNN (red), GBR (sky blue), and SVR (dark blue), alongside the MD reference results (black lines).

Across all systems, RFR consistently yielded the closest agreement with MD simulations, closely tracking both the peak intensities and the short-term fluctuations. This fidelity was particularly evident in ethanol cases such as C3 and C5 (5% and 10% ethanol shown in Figs. 10(c) and (e), where RFR closely captured the onset of NO formation and subsequent oscillatory behaviour. FCNN, benefiting from deep learning architecture and multi-layer abstraction, also demonstrated high predictive accuracy at both low and high temperature scenarios, with performance standing as the second place only after RFR. For example, in C2 (0% Alc. at 3,000 K in Fig. 10(b)), FCNN closely followed MD dynamics during both the peak and relaxation phases. SVR and GBR, by contrast, showed significant deviation in most cases. SVR often underpredicted rapid transitions (e.g., C7, 5% methanol in Fig. 10(f)), while GBR exhibited over-smoothing and lagged behind MD trends, failing to handle the occasional NO_x

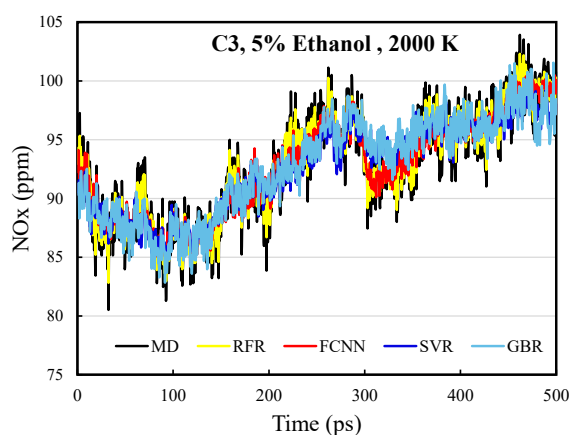
shifts in methanol-rich systems such as C10 (see Fig. 10(j)). The ensemble method used in RFR enables real-time, adaptable responses to sudden changes, showcasing vital capacity of monitoring transient combustion chemistry. FCNN is ideal for systems with complex alcohol–radical interactions because it can model highly intricate non-linear relationships. In contrast, SVR’s fixed kernel design and GBR’s reliance on a sequence of shallow learners limit their adaptability in fast-changing chemical environments such as the rapid NO_x fluctuations occurring during combustion.



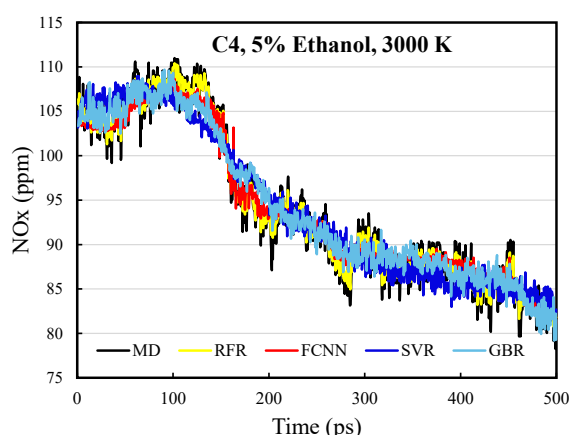
(a)



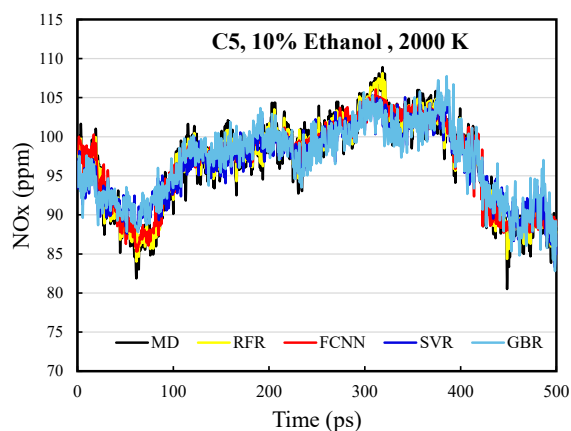
(b)



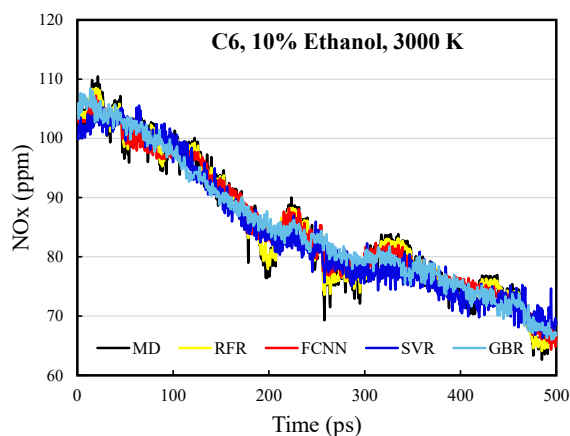
(c)



(d)



(e)



(f)

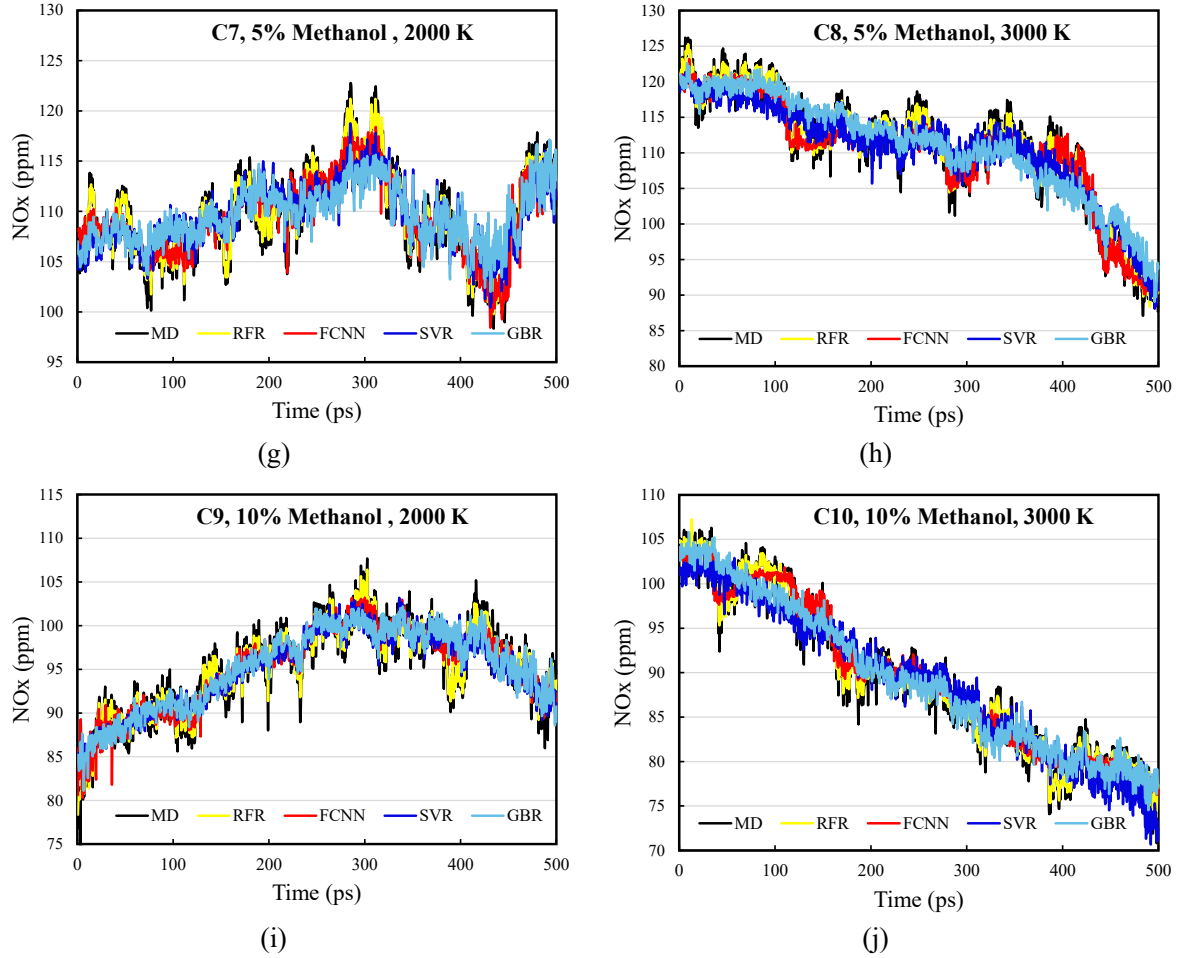


Fig. 10 Comparison of NO_x evolution predicted by four ML models (e.g., RFR, FCNN, SVR, and GBR) against ReaxFF MD data for 10 combustion cases (C1–C10) at 2,000 K and 3,000 K: (a) C1 at 2,000 K; (b) C2 at 3,000 K; (c) C3 at 2,000 K; (d) C4 at 3,000 K; (e) C5 at 2,000 K; (f) C6 at 3,000 K; (g) C7 at 2,000 K; (h) C8 at 3,000 K; (i) C9 at 2,000 K; and (j) C10 at 3,000 K.

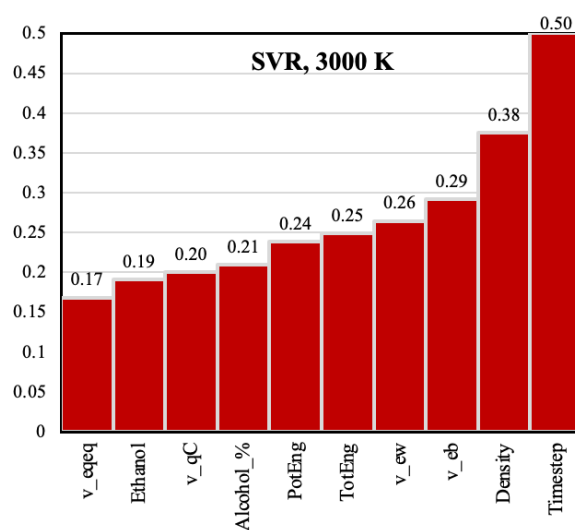
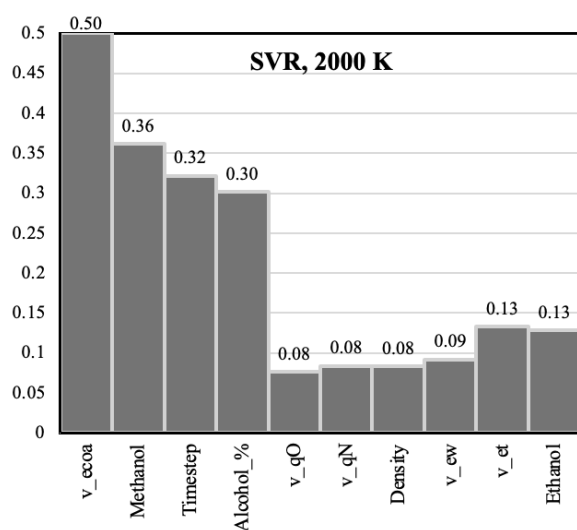
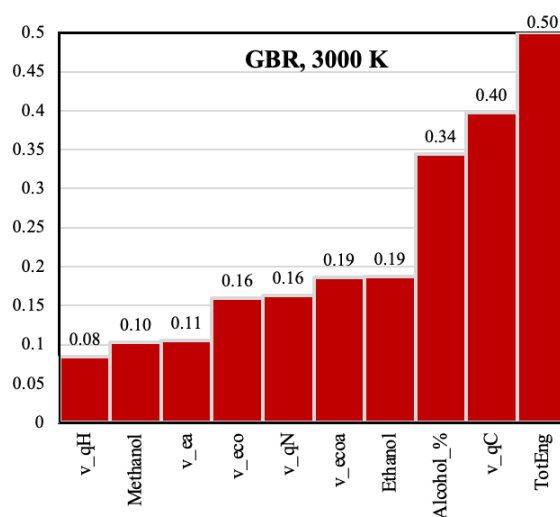
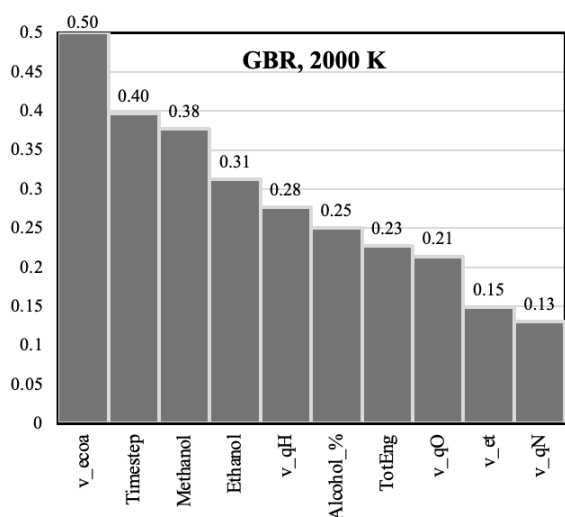
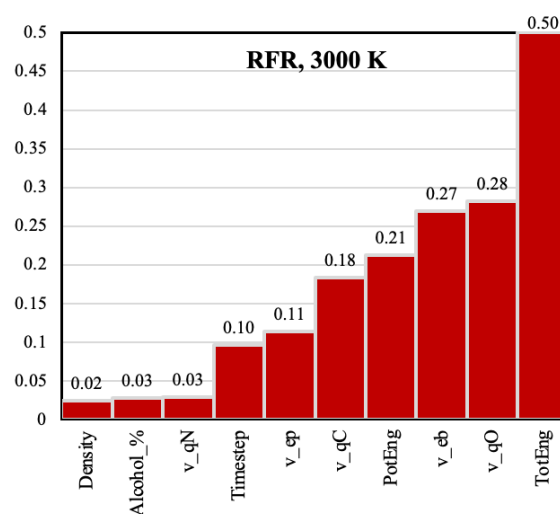
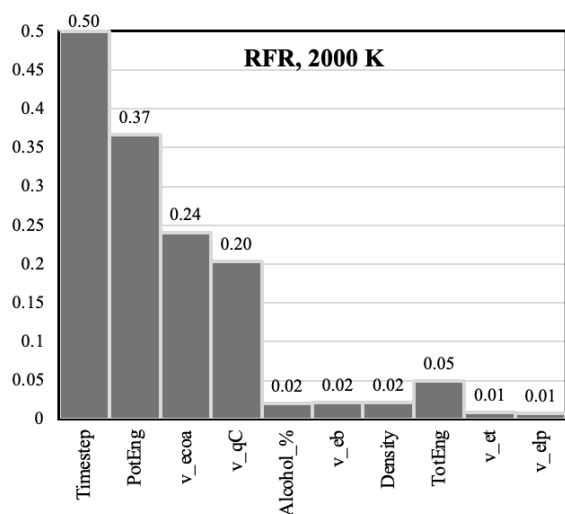
Tables 4 and 5 display a direct comparison of NO_x emissions between ML model predictions and MD simulation results in the base fuel systems, C1 at 2,000 K and C2 at 3,000 K, which complement the previously discussed performance metrics and learning curves. The analysis reports ten separate time steps ranging from 50 to 500ps to consider the complete trajectory span. The RFR model demonstrates superior accuracy through its lowest recorded average absolute and relative errors at every time step. RFR exhibited the lowest error margins, with percentage errors consistently below 1.6% at 2,000 K (see Table 4) and under 1% for most time steps at 3,000 K (see Table 5). For instance, RFR predicted 86.896ppm vs. 87.883ppm in MD at 250ps, reporting an absolute error of only 0.987ppm (1.12%). FCNN also maintained strong accuracy with errors generally under 2.5%, occasionally outperforming RFR at later time steps, such as at 500ps in C2 in Table 5, where it only had an error of 0.14ppm. SVR and GBR showed good performance but displayed minor over- or under-predictions of NO_x during longer reaction periods (e.g., 300–500ps) which aligns with findings from predicted–actual plots (Figs. 8) and sensitivity analysis (Fig. 11). For example, at 300ps in C1 in Table 4, the reported error by SVR reached 5.707ppm (6.15%), which was closely followed by GBR. This quantitative evaluation supports the observed trends from the performance plots specifically the actual vs. predicted correlations in Fig. 8, the learning curves in Fig. 9, and the NO_x evolution patterns predicted by the four ML models, as shown in Fig. 10, reinforce the

established performance hierarchy: RFR2 > FCNN2 > GBR4 \approx SVR1., with RFR2 and FCNN2 emerging as the most effective configurations (see Table 5). While the results align well with the behaviour observed in physics-based simulations, this consistency suggests that machine learning models—particularly ensemble approaches—can capture key patterns in NO_x evolution within ammonia–methane combustion systems when trained appropriately

3.2.3. Sensitivity analysis of key predictors

To deepen understanding of the ML models' decision-making processes, a sensitivity analysis was performed on the most influential predictors contributing to NO_x emission predictions. These predictors were selected based on their normalised importance scores within the best-performing architecture of each model: RFR2, SVR1, GBR4, and FCNN2 (see Fig. 11). It should be noted that only the most impactful variables are shown, not the full feature set of 26 inputs. The RFR2 model identifies Timestep along with PotEng (potential energy) and v_ecoa (valence angle conjugation energy) as the leading three contributors at 2,000 K, followed by v_qC (partial charge on C atoms). Timestep and PotEng are physically intuitive parameters because they represent the reactive system's dynamic and thermodynamic evolution. The v_qC measurement shows how C atoms participate in oxidation reactions with OH and O radicals when alcohol additives are present. The RFR model's internal weighting aligns with known chemical kinetics, showing its high interpretability and reliability. At 3,000 K, RFR2 places even greater weight on TotEng (total system energy), v_qO (partial charge on O atoms), and v_eb (bond energy), all of which are strongly correlated with high-temperature reactivity. The appearance of v_ep (Coulombic interaction energy) and v_eqeq (charge equilibration energy) further confirms that charge redistribution becomes a dominant mechanism in NO_x formation under elevated temperatures, which is consistent with conclusions supported by MD results in Sec. 3.1. For GBR4 model, the pattern is similar but places more emphasis on electron-specific descriptors. At 2,000 K, v_ecoa, Timestep, and both alcohol types (methanol and ethanol) play leading roles. At 3,000 K, TotEng, v_qC, and mass fraction of alcohol are primary, followed by v_ecoa, v_eco (conjugation energy), and v_ca (atom-centred charge energy). These findings suggest that GBR captures both global thermodynamic trends and local charge effects, despite corresponding less direct relation to combustion chemistry compared with RFR2. The SVR1 model, while achieving decent performance, relies more heavily on high-level variables such as methanol, mass fraction of alcohol, and Timestep, which are the most influential at 2,000 K. At 3,000 K, the shift toward Timestep, Density, and TotEng shows that SVR1 responds more to global system states than fine-grained chemical details. Notably, features such as v_eqeq, v_qC, and v_ew (van der Waals energy) also appear, indicating that SVR1 can detect some electronic effects, though less consistently. The FCNN2 model, representing a deep learning approach, reveals a distinct pattern of feature prioritization. At 2,000 K, the most influential features include Methanol and Alcohol_% dominate, followed by v_ecoa, Timestep, and v_qC. At 3,000 K, the model assigns highest importance to Timestep, Alcohol_%, v_qC, PotEng, and lower-level features such as v_ep and v_elp (lone-pair energy). FCNN2 appears to focus more on general system reactivity and alcohol input terms, potentially due to its capacity to encode nonlinear relationships across broad feature spaces. This aligns with typical deep learning behaviour, where low-level patterns are distributed across multiple internal layers rather than interpreted individually. Among all models, RFR demonstrates the strongest alignment between its predictive logic and the underlying combustion mechanisms. Its preference for chemically meaningful variables such as v_qO, v_qC, PotEng, and v_ecoa reinforces its status

as the most chemically interpretable model in this study. Its ability to shift emphasis from carbon-related dynamics at 2,000 K to oxygen and total energy at 3,000 K reflects the actual behaviour of NO_x precursors and formation pathways observed in MD simulations.



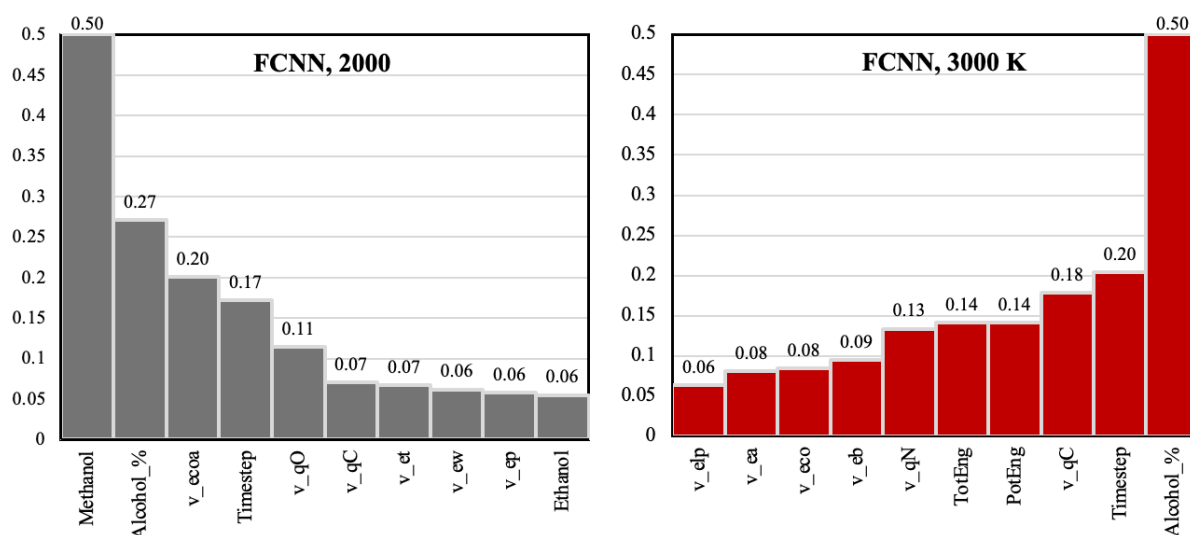


Fig. 11 Sensitivity analysis of the most influential input features for NO_x prediction among the best-performing models (RFR2, GBR4, SVR1, and FCNN2) at 2,000 K and 3,000 K. Variable importance values are normalised to highlight the key contributions from physical, chemical and electronic descriptors.

Table 4 Comparison of NOx emissions between ML model predictions and MD simulation results at 2,000 K (System C1, 0% Alcohol).

Output	System	Temp.	Time (ps)	MD	RFR	RFR Abs. error	RFR percentage error	FCNN	FCNN Abs. error	FCNN percentage error	SVR	SVR Abs. error	SVR percentage error	GBR	GBR Abs. error	GBR percentage error
NOx (ppm)	C1	2000 K	50	77.852	78.892	1.040	1.336	82.643	4.791	6.154	82.103	4.251	5.460	81.592	3.739	4.803
			100	89.812	85.155	4.658	5.186	85.066	4.746	5.284	85.003	4.809	5.355	85.260	4.552	5.068
			150	86.782	86.584	0.198	0.228	85.227	1.555	1.792	84.225	2.558	2.947	84.381	2.401	2.767
			200	91.031	91.582	0.552	0.606	92.155	1.124	1.235	90.330	0.700	0.769	90.757	0.274	0.300
			250	87.883	86.896	0.987	1.123	85.058	2.824	3.214	86.061	1.822	2.073	86.515	1.367	1.556
			300	92.867	87.341	5.526	5.951	86.412	6.455	6.951	87.160	5.707	6.145	88.286	4.581	4.933
			350	87.719	86.873	0.846	0.965	84.628	3.091	3.524	86.669	1.050	1.197	86.440	1.279	1.458
			400	89.310	88.941	0.369	0.413	87.765	1.545	1.730	87.570	1.740	1.948	88.226	1.084	1.213
			450	83.888	85.239	1.350	1.610	88.963	5.074	6.049	87.737	3.849	4.588	87.896	4.008	4.778
			500	90.788	90.189	0.599	0.660	90.576	0.212	0.233	87.893	2.895	3.189	87.107	3.680	4.054

Table 5 Comparison of NOx emissions between ML model predictions and MD simulation results at 3,000 K (System C2, 0% Alcohol).

Output	System	Temp.	Time (ps)	MD	RFR	RFR Abs. error	RFR Percentage error	FCNN	FCNN Abs. error	FCNN Percentage error	SVR	SVR Abs. error	SVR Percentage error	GBR	GBR Abs. error	GBR Percentage error
NOx (ppm)	C2	3000 K	50	99.89	99.84	0.04	0.04	99.66	0.23	0.23	99.22	0.66	0.66	102.68	2.80	2.80
			100	103.06	101.62	1.43	1.39	101.24	1.81	1.76	97.45	5.61	5.44	99.62	3.44	3.34
			150	97.75	97.00	0.76	0.78	96.53	1.22	1.25	94.05	3.70	3.78	95.60	2.15	2.20
			200	92.03	91.48	0.55	0.60	90.54	1.49	1.62	91.18	0.85	0.93	91.50	0.54	0.58
			250	89.40	89.41	0.01	0.01	90.48	1.08	1.21	89.92	0.51	0.57	87.61	1.80	2.01
			300	83.70	85.84	2.14	2.56	85.90	2.19	2.62	87.64	3.94	4.71	84.57	0.87	1.04
			350	83.06	82.84	0.22	0.26	81.85	1.21	1.45	82.53	0.53	0.64	83.96	0.90	1.08
			400	78.75	78.17	0.58	0.74	79.15	0.41	0.52	79.28	0.53	0.67	78.51	0.24	0.31
			450	80.39	79.96	0.43	0.54	79.42	0.97	1.20	75.53	4.85	6.03	77.99	2.39	2.98
			500	76.84	77.37	0.53	0.69	76.70	0.14	0.18	72.54	4.31	5.60	77.20	0.36	0.46

3.3. Extrapolative predictions for untrained alcohol ratios

Extrapolation, in this context, refers to the model's ability to make reliable predictions for input conditions, here, alcohol concentrations that lie outside the numerical range seen during training. Unlike interpolation, which estimates values between known data points, extrapolation tests whether the model has truly learned the underlying chemical relationships that generalize to unobserved systems. The ability to perform such extrapolative prediction is crucial for real-world combustion research, as it enables low-cost virtual screening of fuel blends without requiring additional expensive and time-consuming simulations. It reflects the model's capacity to generalize beyond known data while still remaining chemically consistent. Fig. 12 shows the ML-predicted NO_x profiles for untrained alcohol concentrations, e.g., 2%, 7%, and 12% of both ethanol and methanol at 2,000 K (see Fig. 12(a)) and 3,000 K (see Fig. 12(b)). These systems (C11–C22) were not included in the original training data, meaning they represent a direct test of the model's extrapolation capability. At 2,000 K in Fig. 12(a), the 2% methanol case in C17 yields the highest NO_x production, surpassing 110ppm at 500ps. In contrast, 2% ethanol in C15 closely tracks the baseline behaviour of C1, stabilising around 90–95ppm. As concentration increases, this disparity narrows: 7% methanol in C21 maintains higher NO_x than 7% ethanol in C19, while at 12% concentration, methanol in C13, grey and ethanol in C11 converge around 95ppm. These results align with earlier MD findings, reaffirming that methanol's aggressive early oxidation at lower temperatures fosters NO_x, while ethanol moderates the release of N-containing radicals. The trend shifts greatly at 3,000 K in Fig. 12(b). All systems exhibit reduced NO_x formation, but now ethanol-rich blends dominate the suppression. The 12% ethanol case in C12 falls below 70ppm in the end, marking the lowest NO_x level among all tested extrapolated cases. Meanwhile, 12% methanol in C14 levels off just under 80ppm. Across mid-level concentrations, 7% ethanol in C20 also outperforms 7% methanol in C22. The low-concentration region again favours ethanol: C16 (2% ethanol) outperforms C18 (2% methanol) by a visible margin.

These trends reinforce two interpretations of the underlying chemical reaction mechanisms. First, methanol is more reactive at low temperatures, likely accelerating NH₃ oxidation through earlier radical generation, which in turn drives NO formation. However, as temperature increases, ethanol's slower and more controlled radical propagation favours routes that stabilise intermediates or divert nitrogen away from NO/NO₂ loops. Second, the model's ability to recover these patterns, despite having been trained solely on 0%, 5%, and 10% alcohol levels, demonstrates the capacity of chemical-guided ML. Although no MD simulations were run for these off-design systems, the trends match known combustion behaviours, illustrating that the model is capable of capturing real chemical logic and reliable for low-cost predictive screening.

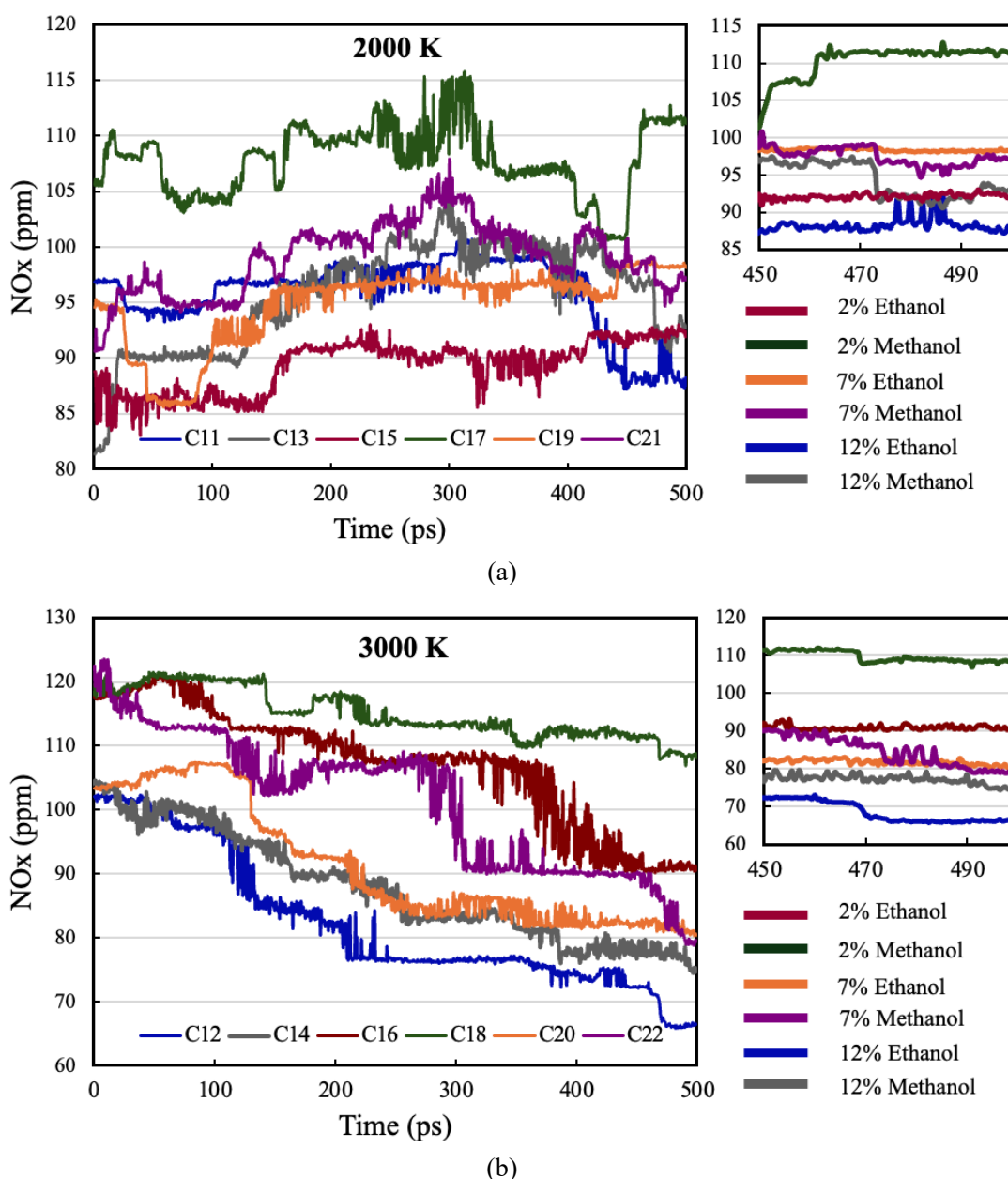


Fig. 12 ML-predicted NO_x emissions for extrapolated alcohol concentrations (2%, 7%, and 12%) of methanol-ethanol in ammonia-methane combustion at: (a) 2,000 K and (b) 3,000 K. The colour codes are: dark red (C15, C16) for 2% ethanol, dark green (C17, C18) for 2% methanol, orange (C19, C20) for 7% ethanol, purple (C21, C22) for 7% methanol, dark blue (C11, C12) for 12% ethanol, and grey (C13, C14) for 12% methanol.

In Tables 6 and 7, predicted values are compared with synthesised ReaxFF MD datasets to validate the extrapolation results for 12% alcohol scenarios. These datasets were predicted for C11, C13 at 2,000 K and C12, C14 at 3,000 K, representing 12% ethanol and 12% methanol, respectively. The results are summarised in terms of absolute and percentage errors for each 100ps period across 500ps. The average percentage error for ethanol is relatively low, increasing from 3.845% at 100ps, to 4.49% at 500ps. The prediction remains stable, but the trend shows an incremental increase in error with time, reflecting the complexity of extrapolation. The percentage error begins at 2.02% when measured at 100ps and increases to 12.78% at 400ps. The rising error trend arises from methanol's increased reactivity, leading to

more significant departures from MD results. The percentage error for 3,000 K cases in Table 7 begins at 6.58% at 100ps and decreases to 5.97% at 500ps as the timestep increases. It suggests the model's predictions stabilize as the combustion dynamics approach the steady state at higher temperatures. In addition, a similar error pattern with methanol is observed. The error starts at 3.26% at 100ps but increases significantly to 17.74% at 400ps. The substantial error rise during intermediate timesteps underscores the difficulties in extrapolating results for high methanol concentrations and elevated temperatures. It can be concluded that increased prediction errors in methanol are due to its stronger reactivity that creates complex reaction pathways, making predictive process more challenging for ML models.

Table 6 Quantitative comparison of RFR model predictions for 12% alcohol concentrations at 2,000 K (cases C11 and C13).

Output	System	Temp.	Time (ps)	Alc. %	Alc. type	MD	ML	Abs. error	Percentage error
NO _x (ppm)	C11	2000 K	100	12%	Ethanol	91.061	94.908	3.847	4.225
	C11	2000 K	200	12%	Ethanol	105.141	98.170	6.971	6.630
	C11	2000 K	300	12%	Ethanol	109.811	99.385	10.426	9.494
	C11	2000 K	400	12%	Ethanol	101.188	96.625	4.563	4.509
	C11	2000 K	500	12%	Ethanol	83.330	87.818	4.488	5.386
	C13	2000 K	100	12%	Methanol	87.706	89.726	2.020	2.303
	C13	2000 K	200	12%	Methanol	88.135	95.456	7.321	8.306
	C13	2000 K	300	12%	Methanol	101.925	103.652	1.727	1.695
	C13	2000 K	400	12%	Methanol	87.059	99.838	12.779	14.679
	C13	2000 K	500	12%	Methanol	88.026	92.682	4.656	5.289

Table 7 Quantitative comparison of RFR model predictions for 12% alcohol concentrations at 3,000 K (cases C12 and C14).

Output	System	Temp.	Time (ps)	Alc. %	Alc. type	MD	ML	Abs. error	Percentage error
NO _x (ppm)	C12	3000 K	100	12%	Ethanol	91.837	98.422	6.584	7.169
	C12	3000 K	200	12%	Ethanol	70.915	82.390	11.475	16.181
	C12	3000 K	300	12%	Ethanol	69.590	76.338	6.749	9.698
	C12	3000 K	400	12%	Ethanol	70.112	74.099	3.987	5.687
	C12	3000 K	500	12%	Ethanol	60.390	66.358	5.968	9.883
	C14	3000 K	100	12%	Methanol	97.138	100.400	3.262	3.359
	C14	3000 K	200	12%	Methanol	83.728	90.587	6.860	8.193
	C14	3000 K	300	12%	Methanol	74.588	83.787	9.199	12.333
	C14	3000 K	400	12%	Methanol	65.553	77.181	11.628	17.738
	C14	3000 K	500	12%	Methanol	71.582	74.921	3.339	4.664

Fig. 13 illustrates the mean percent error in ML model predictions for several alcohol concentrations, showing the acceptable margin of error (e.g., $\leq 5\%$ for several cases such as C15, C16, and C18) reflects the robustness of RFR model in predicting NO_x emissions for extrapolated cases within reasonable error limits. The ethanol-rich systems exhibit lower average percentage errors, with C11 (12% ethanol at 2,000 K) showing the smallest error (5.33%), while the methanol-rich systems (C13) show the largest error (12.85%) at 2,000 K.

At 3,000 K, the trend persists, with ethanol systems maintaining lower error levels compared with methanol, reflecting ethanol's relatively stable behaviour at higher temperatures. In 2,000 K, the error for methanol tends to increase at higher concentrations, particularly in cases (C17) of 12% methanol. This trend matches what is shown in Tables 6 and 7, where mixtures with methanol have larger errors, both in total amount and percentage, than those with ethanol. The larger errors in methanol-rich systems happen because methanol reacts more in cold conditions, making it harder for models to accurately predict the detailed reaction processes. In contrast, ethanol-rich systems, while still presenting some extrapolative challenges, exhibit more consistent model behaviour, particularly at higher temperatures such as 3000 K.

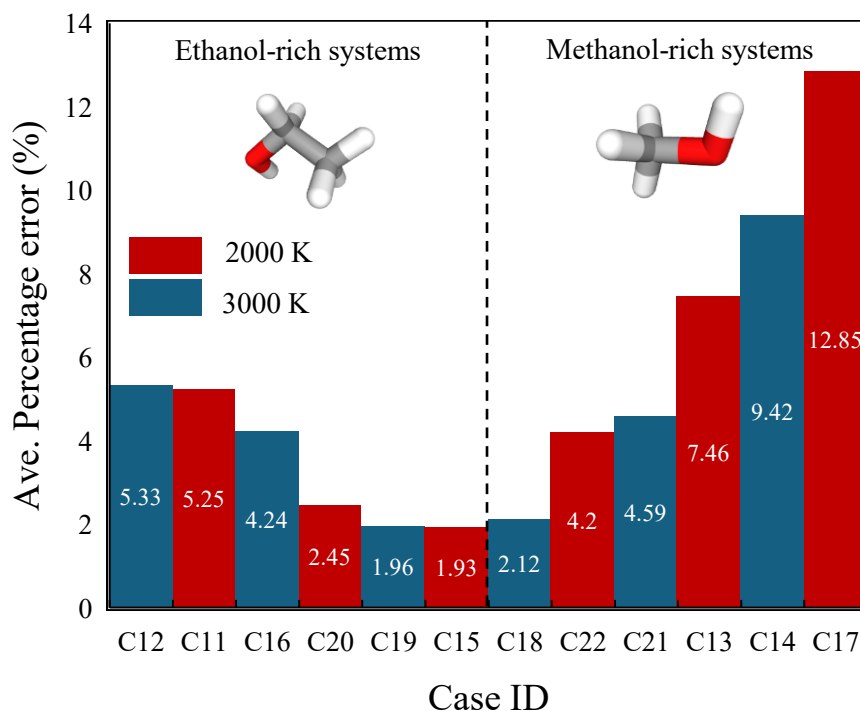


Fig. 13 Average percentage error of RFR-predicted NO_x emissions across extrapolated alcohol concentrations (2%, 7%, and 12%) for different ammonia-methane-alcohol combustion cases (C11-C22) at 2,000 K (red bars) and 3,000 K (blue bars).

While the extrapolation to 12% alcohol is successfully achieved with acceptable accuracy, the extrapolation to higher percentages of alcohol (e.g., 15–20%) is difficult. The increased reactivity and complexity of chemical pathways at higher concentrations make it difficult to maintain high predictive accuracy. When alcohol levels get close to 15–20%, the way the fuel and air mix reacts can change significantly compared with the data used to train the model, leading to bigger differences between what the model predicts and the actual combustion outcomes. This limitation likely stems from a lack of representative training samples capturing the altered charge distributions, energy profiles, and species interaction dynamics unique to these higher alcohol blends. Further work is needed to enhance the extrapolation process, particularly to 15–20% alcohol levels, which may need more training data or better feature chemical reactions to capture non-linear effects at those levels. These non-linearities arise from threshold-driven changes in radical formation, bond dissociation patterns, and secondary reactions that do not scale linearly with alcohol concentration. For example, higher hydroxyl content at $\geq 15\%$ alcohol may shift dominant NO_x formation pathways or trigger new intermediate stabilization loops not seen at lower concentrations.

4. Conclusions

This study employed ReaxFF-based molecular dynamics simulations to investigate the impact of ethanol and methanol additives at concentrations of 0%, 5%, and 10% on the combustion behaviour of ammonia–methane mixtures under high-temperature conditions (2,000 K and 3,000 K). The results demonstrated that alcohol enrichment strongly alters charge redistribution, NO_x formation, and intermediate stability. At 2,000 K, methanol-rich mixtures (especially C7 and C9) exhibited pronounced electron withdrawal from nitrogen atoms, accelerated NH₃ oxidation, and elevated NO_x levels, with C7 reaching 110.54 ppm. In contrast, 10% ethanol (C5) suppressed NO_x more effectively, producing only 88.31 ppm compared to 90.79 ppm in the base fuel. At 3,000 K, ethanol showed even stronger NO_x-reduction performance particularly in C6 (10% ethanol), which achieved the lowest NO_x level of 66.46 ppm, reflecting a 39.5% decrease compared to C2 (109.95 ppm). Methanol's performance at high temperature was moderate (C10: 76.84 ppm), due to sustained reactivity and enhanced radical production. Charge equilibration analysis revealed more stable electron distributions in methanol cases at 2,000 K and greater reactivity in ethanol-rich mixtures at 3,000 K. The dominant reaction pathways also shifted: ethanol favoured reversible NO₂ \rightleftharpoons HNO₃ loops at low temperatures and nitrate decomposition at high temperatures, while methanol facilitated NO conversion through HNO and N₂O routes. These findings underline that both alcohol type and concentration play pivotal roles in modulating NO_x pathways and combustion reactivity. Four regression models were trained with the atomistic descriptors from MD simulations, including Random Forest Regression (RFR), Support Vector Regression (SVR), Gradient Boosting Regression (GBR), and Fully Connected Neural Networks (FCNN). Among these, the RFR2 model (a tree-based ensemble method) achieved the highest accuracy, with a Mean Absolute Error (MAE) of 0.661 and R² of 0.993, followed by FCNN2 (MAE \approx 1.74–2.04, R² = 0.940). GBR4 showed moderate accuracy, while SVR1 had the weakest performance (MAE = 2.285, R² = 0.903). The RFR model accurately predicted NO_x formation within the interpolated range (2%, 5%, 7%, and 10%) as well as for extrapolated alcohol levels (12%), with errors <5% for ethanol-rich mixtures and moderate errors in methanol-rich mixtures. This framework provides a novel predictive route that bypasses the need for direct simulations at every blend ratio, enabling scalable exploration of fuel compositions. Quantitative validation against synthetic MD data showed low prediction errors (\leq 5%) in most ethanol cases and moderate errors in methanol-rich systems. The results indicate that extrapolation within the 10–12% range is numerically viable, whereas predictions over 15% may necessitate enhanced models or broader datasets to improve the accuracy. It is because the models could not capture the fundamentally altered reaction dynamics and bond dissociation mechanisms observed in that regime. Future work will aim to enhance the extrapolative robustness of the ML models by integrating noise-reduced, chemically valid training data [51] and incorporating reaction-aware physical priors [52] to better capture transition dynamics. In addition, emerging frameworks such as optimal transport for reaction state mapping [53], physics-informed neural networks for reaction–diffusion systems [52], and language-model-driven chemical embedding techniques [54] offer promising pathways to generalize the current approach toward broader chemical regimes, including transition state estimation and real-time reactive force field tuning [55].

Acknowledgement

The authors express their gratitude to Monolith AI for granting permission to utilize their Monolith platform. Mr. Amirali Shateri likes to acknowledge the University of Derby for the PhD studentship (contract no. S&E_Engineering_0722) and the support provided.

References

- [1] Lü, M., Long, W., Wei, F., Dong, D., Li, C., Dong, P., Tian, H., Chen, X., Chen, S., Wang, Y., & Wang, P. (2024). Assessment of carbon-free fuel ammonia combustion with low methanol blends in reducing GHG emissions including N₂O. *Journal of Cleaner Production*, 463, 142755.
- [2] Lü, M., Long, W., Wei, F., Dong, D., Li, C., Dong, P., Tian, H., Chen, X., Chen, S., Wang, Y., & Wang, P. (2024). Assessment of carbon-free fuel ammonia combustion with low methanol blends in reducing GHG emissions including N₂O. *Journal of Cleaner Production*, 463, 142755.
- [3] Guo, Y., Shi, H., Liu, H., Xie, Y., & Guan, Y. (2023). Reactive molecular dynamics simulation and chemical kinetic modeling of ammonia/methane co-combustion. *Fuel*.
- [4] Shateri, A., Jalili, B., Saffar, S., Jalili, P., & Ganji, D. D. (2023). Numerical study of the effect of ultrasound waves on the turbulent flow with chemical reaction. *Energy*.
- [5] Liao, W., Wang, Y., & Chu, Z. (2024). Investigating auto-ignition characteristics and kinetic modeling of NH₃/CH₄ mixtures using an RCM. *Combustion and Flame*.
- [6] Kohansal, M. M., Kiani, M. T., Masoumi, S., Ashjaee, M., & Houshfar, E. (2023). Experimental and Numerical Investigation of NH₃/CH₄ Mixture Combustion Properties under Elevated Initial Pressure and Temperature. *Energy & Fuels*.
- [7] Singh, A. S., Vijrumbana, Y., & Reddy, V. M. (2023). Experimental and computational (Chemical Kinetic + CFD) analyses of Self-Recuperative annular tubular porous burner for NH₃/CH₄ -air Non-Premixed combustion. *Chemical Engineering Journal*.
- [8] Kim, G. T., Park, J. G., Chung, S. H., & Yoo, C. S. (2023). Synergistic effect of non-thermal plasma and CH₄ addition on turbulent NH₃/air premixed flames in a swirl combustor. *International Journal of Hydrogen Energy*.
- [9] Chu, X., X, L., Gao, P., Ma, Z., Xiao, H., Xie, C., Zhang, Z., & Wang, X. (2024). High-temperature auto-ignition characteristics of NH₃-H₂-CH₄. *Fuel*, 365, 131228.
- [10] Zhang, J., Mei, B. W., Liu, W., Fang, J., Zhang, Y., Cao, C., & Li, Y. (2022). Unraveling Pressure Effects in Laminar Flame Propagation of Ammonia: A Comparative Study with Hydrogen, Methane, and Ammonia/Hydrogen. *Energy & Fuels*, 36(15), 8528–8537.
- [11] Han, X., Feng, H., Lin, R., & Konnov, A. A. (2024). A new correlation between diluent fraction and laminar burning velocities: Example of CH₄, NH₃, and CH₄ + NH₃ flames diluted by N₂. *Fuel*.
- [12] Usman, M., Malik, M. A. I., Chaudhary, T. N., Riaz, F., Raza, S., Abubakar, M., Ahmad, H. M., Fouad, Y., Abbas, M., & Kalam, Md. A. (2023). Comparative Assessment of Ethanol and Methanol–Ethanol Blends with Gasoline in SI Engine for Sustainable Development. *Sustainability*, 15(9), 7601.

- [13] Yu, M., Zhan, J.-H., Li, X., He, W., & Liu, X. (2023). Effect of methanol on the pyrolysis behaviour of kerogen by ReaxFF molecular dynamics simulations. *Molecular Simulation*.
- [14] Shateri, A., Yang, Z., & Xie, J. (2025). Machine Learning-Based Molecular Dynamics Studies on Predicting Thermophysical Properties of Ethanol–Octane Blends. *Energy & Fuels*.
- [15] Mao, G.-P., Shi, T., Mao, C., & Wang, P. (2023). Prediction of NO_x emission from two-stage combustion of NH₃–H₂ mixtures under various conditions using artificial neural networks. *International Journal of Hydrogen Energy*.
- [16] Shin, Y., Kim, Z., Yu, J., Kim, G., & Hwang, S. (2019). Development of NO_x reduction system utilizing artificial neural network (ANN) and genetic algorithm (GA). *Journal of Cleaner Production*, 232, 1418–1429.
- [17] Hoque, K. E., Hossain, T., Haque, A. M., Miah, Md. A. K., & Haque, Md. A. (2024). NO_x Emission Predictions in Gas Turbines through Integrated Data-Driven Machine Learning Approaches. *Journal of Energy Resources Technology-Transactions of The Asme*.
- [18] Pachauri, N. (2024). An emission predictive system for CO and NO_x from gas turbine based on ensemble machine learning approach. *Fuel*.
- [19] Adams, D., Oh, D. H., Kim, D. W., Lee, C. H., & Oh, M. (2020). Prediction of SO_x–NO_x emission from a coal-fired CFB power plant with machine learning: Plant data learned by deep neural network and least square support vector machine. *Journal of Cleaner Production*, 270, 122310.
- [20] Shateri, A., Yang, Z., & Xie, J. (2024). Utilizing Artificial intelligence to identify an Optimal Machine learning model for predicting fuel consumption in Diesel engines. *Energy and AI*.
- [21] Shateri, A., Yang, Z., Liu, Y., & Xie, J. (2025). Data-driven optimization of turbulent kinetic energy and tumble-y in combustion engines: A comparative study of machine learning models. *Fuel*, 389, 134590.
- [22] Mueller, J. E., van Duin, A. C. T., & Goddard, W. A. (2010). Application of the ReaxFF Reactive Force Field to Reactive Dynamics of Hydrocarbon Chemisorption and Decomposition. *Journal of Physical Chemistry C*, 114(12), 5675–5685.
- [23] Wang, Q.-D., Wang, J.-B., Li, J.-Q., Tan, N.-X., & Li, X.-Y. (2011). Reactive molecular dynamics simulation and chemical kinetic modeling of pyrolysis and combustion of n-dodecane. *Combustion and Flame*, 158(2), 217–226.
- [24] Mao, Q., Yang, M. D., Wei, C., Liu, X., Jiang, X., Ren, Y., Luo, K. H., & van Duin, A. C. T. (2023). Classical and reactive molecular dynamics: Principles and applications in combustion and energy systems. *Progress in Energy and Combustion Science*, 97, 101084.
- [25] Chowdhury, A., & van Duin, A. C. T. (2017). Extension of the ReaxFF Combustion Force Field toward Syngas Combustion and Initial Oxidation Kinetics. *Journal of Physical Chemistry A*, 121(5), 1051–1068.
- [26] van Duin, A. C. T., Dasgupta, S., Lorant, F., & Goddard, W. A. (2001). ReaxFF: A Reactive Force Field for Hydrocarbons. *Journal of Physical Chemistry A*, 105(41), 9396–9409.

- [27] Kulkarni, A. D., Truhlar, D. G., Srinivasan, S. G., van Duin, A. C. T., Norman, P., & Schwartzenuber, T. E. (2013). Oxygen Interactions with Silica Surfaces: Coupled Cluster and Density Functional Investigation and the Development of a New ReaxFF Potential. *Journal of Physical Chemistry C*, 117(1), 258–269.
- [28] Zhang, L., Zybin, S. V., van Duin, A. C. T., Dasgupta, S., Goddard, W. A., & Kober, E. M. (2009). Carbon cluster formation during thermal decomposition of octahydro-1,3,5,7-tetranitro-1,3,5,7-tetrazocine and 1,3,5-triamino-2,4,6-trinitrobenzene high explosives from ReaxFF reactive molecular dynamics simulations. *Journal of Physical Chemistry A*, 113(40), 10619–10640.
- [29] Xu, Y., Mao, Q., Wang, Y., Luo, K. H., Zhou, L., Wang, Z., & Wei, H. (2023). Role of ammonia addition on polycyclic aromatic hydrocarbon growth: A ReaxFF molecular dynamics study. *Combustion and Flame*, 250, 112651.
- [30] Wang, J., Jiang, X. Z., & Luo, K. H. (2023). Exploring reaction mechanism for ammonia/methane combustion via reactive molecular dynamics simulations. *Fuel*, 331, 125806.
- [31] Chenoweth, K., van Duin, A. C. T., & Goddard, W. A. (2008). ReaxFF Reactive Force Field for Molecular Dynamics Simulations of Hydrocarbon Oxidation. *Journal of Physical Chemistry A*, 112(5), 1040–1053.
- [32] Bauschlicher, C. W., & Langhoff, S. R. (1991). Theoretical study of the CH bond dissociation energies of CH₄, C₂H₂, C₂H₄, and H₂C₂O. *Chemical Physics Letters*, 177(2), 133–138.
- [33] Jursic, B. S. (1996). The evaluation of nitrogen containing bond dissociation energies using the ab initio and density functional methods. *Journal of Molecular Structure-Theochem*, 366, 103–108.
- [34] Plimpton, S. J. (1995). Fast parallel algorithms for short-range molecular dynamics. *Journal of Computational Physics*, 117(1), 1–19.
- [35] Martínez, L., Andrade, R., Birgin, E. G., & Martínez, J. M. (2009). PACKMOL: A package for building initial configurations for molecular dynamics simulations. *Journal of Computational Chemistry*, 30.
- [36] Döntgen, Malte, et al. "Automated discovery of reaction pathways, rate constants, and transition states using reactive molecular dynamics simulations." *Journal of chemical theory and computation* 11.6 (2015): 2517-2524.
- [37] Stukowski, A. (2010). Visualization and analysis of atomistic simulation data with OVITO—the Open Visualization Tool. *Modelling and Simulation in Materials Science and Engineering*, 18(1), 015012.
- [38] Ihme, M., Chung, W. T., & Mishra, A. (2022). Combustion machine learning: Principles, progress and prospects. *Progress in Energy and Combustion Science*, 91, 101010.
- [39] Willmott, C. J., & Matsuura, K. (2005). Advantages of the mean absolute error (MAE) over the root mean square error (RMSE) in assessing average model performance. *Climate Research*, 30(1), 79–82.

- [40] Chai, T., Chai, T., & Draxler, R. R. (2014). Root mean square error (RMSE) or mean absolute error (MAE)? – Arguments against avoiding RMSE in the literature. *Geoscientific Model Development*, 7(3), 1247–1250.
- [41] Mu, Y., Liu, X., & Wang, L. (2018). A Pearson’s correlation coefficient based decision tree and its parallel implementation. *Information Sciences*, 435, 40–58.
- [42] Draper, N. R., & Smith, H. (1998). *Applied regression analysis* (Vol. 326). John Wiley & Sons.
- [43] Zapiain, D. M. de O., Venkatraman, A., & Wilson, M. (2024). *Accelerating Charge Estimation in Molecular Dynamics Simulations Using Physics-Informed Neural Networks: Corrosion Applications*.
- [44] Borodin, A., Höfft, O., Kempter, V., Ferro, Y., & Allouche, A.-R. (2004). Electron delocalization by polar molecules: interaction of Na atoms with solid ammonia films studied with MIES and density functional theory. *Journal of Chemical Physics*, 121(8), 3717–3721.
- [45] Hill, S. C., & Smoot, L. D. (2000). Modeling of nitrogen oxides formation and destruction in combustion systems. *Progress in energy and combustion science*, 26(4-6), 417-458.
- [46] Watson, G. M. G., Versailles, P., & Bergthorson, J. M. (2017). *NO formation in rich premixed flames of C1–C4 alkanes and alcohols*. 36(1), 627–635.
- [47] Gao, Y., Guo, Y., Xie, Y., Qin, H., & Guan, Y. (2024). Kinetic mechanism and NO_x emission characteristics of the ammonia/alcohol co-combustion explored by reactive molecular dynamics calculation and kinetic numerical simulation. *Combustion and Flame*, 273, 113953.
- [48] Song, L., Xu, C.-C., Ye, J., Zhang, Y., Chen, B., Hou, F. F., Chen, B.-C., Su, H., & Sun, J. (2024). Pyrolysis and oxidation mechanisms of ethylene and ethanol blended fuel based on ReaxFF molecular dynamics simulation. *Fuel*, 373, 132361.
- [49] Wang, Y., Mao, Q., Wang, Z., Luo, K. H., Zhou, L., & Wei, H. (2023). A ReaxFF molecular dynamics study of polycyclic aromatic hydrocarbon oxidation assisted by nitrogen oxides. *Combustion and Flame*, 248, 112571.
- [50] Chen, Z., Sun, W., Zhao, L., & Zhao, L. (2018). Combustion Mechanisms and Kinetics of Fuel Additives: A ReaxFF Molecular Simulation. *Energy & Fuels*, 32(11), 11852–11863.
- [51] Toniato, A., Schwaller, P., Cardinale, A., Geluykens, J., & Laino, T. (2021). Unassisted noise reduction of chemical reaction datasets. *Nature Machine Intelligence*, 3(6), 485-494.
- [52] Rao, C., Ren, P., Wang, Q., Buyukozturk, O., Sun, H., & Liu, Y. (2023). Encoding physics to learn reaction–diffusion processes. *Nature Machine Intelligence*, 5(7), 765-779.
- [53] Duan, C., Liu, G. H., Du, Y., Chen, T., Zhao, Q., Jia, H., ... & Kulik, H. J. (2025). Optimal transport for generating transition states in chemical reactions. *Nature Machine Intelligence*, 7(4), 615-626.
- [54] Jablonka, K. M., Schwaller, P., Ortega-Guerrero, A., & Smit, B. (2024). Leveraging large language models for predictive chemistry. *Nature Machine Intelligence*, 6(2), 161-169.

[55] Gong, S., Zhang, Y., Mu, Z., Pu, Z., Wang, H., Han, X., ... & Xiang, L. (2025). A predictive machine learning force-field framework for liquid electrolyte development. *Nature Machine Intelligence*, 1-10.